Chapter 3
Contact Mechanics

Robert L. Jackson, Hamed Ghaednia, Hyeon Lee, Amir Rostami, and Xianzhang Wang

Abstract Contact mechanics is a fundamental field of tribology and generally refers to the interaction of solid surfaces. This interaction or contact can occur on many different scales, ranging from nanoscale asperities up to tires on roads and even contact between tectonic plates. This chapter reviews the basic technical information available in predicting the contact area, pressure, stresses, and forces that occur when surfaces interact. The chapter considers different geometries such as spheres and wavy surfaces and also outlines how to consider elastic and plastic deformation. The phenomena of creep and adhesion that are important for many tribological applications, and especially biological contacts, are also discussed. Finally, the chapter concludes by covering methods used to model the complicated situation of contact between rough surfaces that contain many different geometrical features.

Nomenclature

a	Radius of circular contact area
A	Area of contact
An	Nominal or apparent area of contact
b	Cylindrical contact half width
B	Aspect ratio
C	Critical yield stress coefficient
Cn	Creep material constant
d	Distance between the mean of the surface peaks and a material and geometry dependent exponent
e	Coefficient of restitution during impact

R.L. Jackson (✉) • H. Ghaednia • H. Lee • A. Rostami • X. Wang
Department of Mechanical Engineering, Auburn University, Auburn, AL, USA
e-mail: jacksr7@auburn.edu

P.L. Menezes et al. (eds.), *Tribology for Scientists and Engineers: From Basics to Advanced Concepts*, DOI 10.1007/978-1-4614-1945-7_3,

e_y	Plastic strain (ratio of yield strength to effective elastic modulus)
E	Elastic modulus
E'	Reduced or effective elastic modulus
f	Spatial frequency (reciprocal of wavelength)
F	Contact force
h	Height of sinusoidal surface from base and distance between the mean of the surface heights
i	Scale or frequency number
I	Statistical contact integral
H	Hardness or normalized layer thickness
L	Length of cylindrical contact
m	Mass of impact sphere
m_n	nth spectral moment of the surface
N	Number of asperities or data points on surfaces
p	Average pressure over entire sinusoidal surface in contact
p^*	Average pressure for complete contact (elastic)
p^*_{ep}	Average pressure for complete contact (elastoplastic)
p_{ave}	Average pressure over entire asperity
P	Spherical contact force
Q_{max}	Tangential load required cause sliding
R	Radius of cylinder or sphere or asperity tip
S_y	Yield strength
t	Time or layer thickness
T	Temperature
V	Velocity
W_{nm}	Work of adhesion between surfaces n and m
x	Lateral surface coordinate
y_s	Distance between the mean of the surface peaks and mean of the surface heights
z	Surface height at location x
α	Layer model parameter and statistical contact parameter
β	Exponential creep material constant and surface roughness parameter
γ_n	Surface energy of surface n
γ_{nm}	Interfacial energy between surfaces n and m
Δ	Amplitude of the sinusoidal surface
δ	Deflection of cylindrical or sinusoidal asperity surface
ε	Strain
θ_a	Adhesion parameter
κ	Layer model parameter
λ	Asperity wavelength or layer model parameter
μ	Effective static friction coefficient
η	Areal asperity density
φ	Asperity height distribution
σ	Normal stress and RMS surface roughness

σ_s	The RMS roughness of the asperity peak heights
v	Poisson's ratio
ω	Deflection or interference of spherical contact
ψ	Plasticity index

Subscripts

o	Initial or at $t = 0$
1, 2	Property for material 1, 2, etc.
c	Critical value at onset of plastic deformation
cr	Creep dependent parameter
a	Elastic area
ep	Elastic-plastic
max	Maximum
n	Normal direction and nominal or apparent area of contact
p	Elastic-plastic or elastic pressure integral
r	Real area of contact
t	Tangential

1 Introduction

Although friction and wear have been the subject of man's thoughts and creations since ancient times, the application of mechanics to contact problems probably first began with Heinrich Hertz (see Fig. 3.1) in solving the problem of elastic deformation between contacting parabolic surfaces. Many have since applied this to the contact of spherical surfaces. Many other well-known researchers have followed in Hertz's footsteps, including, but not limited to, Archard [1], Tabor [2], and Greenwood, and Williamson [3]. However, K. L. Johnson [4] may be the most well-known contemporary in the field and is the author of the seminal book on the subject, "Contact Mechanics."

Contact between solids is undeniably important because it is such a common and critical occurrence in our daily lives, health, in industry, and even on the scale of heavenly bodies and the universe. When two objects are brought together, their matter may initially attract, but as they get closer and closer, the attraction will eventually decrease and turn to repulsion which coincides with our intuitive description of contact. Contacts can and do cause very high stresses between objects that can cause failure in the form of fracture, yielding, surface fatigue, and wear. Predicting these stresses with a great deal of resolution can also be very difficult since surfaces are almost always significantly rough and possess a complicated and perhaps unpredictable geometry. Within these complex interactions, many phenomena such as friction, wear, and contact resistance are governed. Nevertheless, significant progress has been made in solving these problems in a practical manner, but still, many obstacles remain.

Fig. 3.1 Heinrich Hertz

There are analytical methods which in some cases render closed form solutions to contact mechanics problems. Numerical methods are also available which will provide an approximate solution when a closed form solution is not possible. We will concentrate mostly on existing analytical solutions to contact problems. However, methods such as finite elements and elastic superposition can be very powerful tools for contact problems that cannot be solved analytically.

In this chapter, we will begin our summary of some of these useful contact mechanics tools by first discussing the contact of elastic smooth curved surfaces as Hertz first described.

2 Single Peak Contact

2.1 Elastic Cylindrical Contact (Line)

Perhaps the most popular and widely used solution in contact mechanics is the contact of two elastic axisymmetric and parabolic structures, first solved by Heinrich Hertz (see Fig. 3.1), apparently while on his Christmas break over a 125 years ago [5]. Although the solution assumes a parabolic geometry, it can provide a precise approximation of elastic contact between cylinders and spheres. The Hertz solution assumes that the interference is small enough such that the geometry does not change significantly and that the surface interactions are frictionless and only repulsive.

When a cylinder contacts a flat surface, the contact area is initially a line until it grows and becomes a rectangle. The same is also true when two cylinders come into contact and their axes of symmetries are parallel. Therefore, cylindrical contacts are

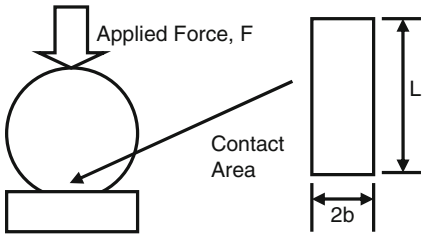

Fig. 3.2 Schematic of the contact area between a cylinder and a flat surface

often referred to as line contacts. A cross section of a cylindrical contact is shown in Fig. 3.2.

Hamrock [6] provides the solution to the deflection of an elastic cylindrical contact:

$$\delta = \frac{F}{\pi E' L}\left[\ln\left(\frac{4\pi E' RL}{F}\right) - 1\right] \tag{3.1}$$

and according to Johnson [4], the half contact width is (the contact area is the cylinder length multiplied by twice the half width)

$$b = \left(\frac{4FR}{\pi LE'}\right)^{1/2} \tag{3.2}$$

Note that E' is often referred to as the equivalent elastic modulus and can be used for the contact of many different surface geometries. E' is given by (each surface is denoted by subscript 1 and 2)

$$\frac{1}{E'} = \frac{1-\nu_1^2}{E_1} + \frac{1-\nu_2^2}{E_2} \tag{3.3}$$

Similarly, R is often referred to as the equivalent radius of curvature and can be used to consider the contact of two spheres with different radii of curvature, denoted R_1 and R_2 here, and calculated by

$$\frac{1}{R} = \frac{1}{R_1} + \frac{1}{R_2} \tag{3.4}$$

Note that contact between a convex and concave surface can also be considered, such as for the contact between a rolling element and a raceway in a bearing by simply making the curvature of the concave surface negative in (3.4).

When the cylinders come into contact, the pressure follows a nearly parabolic profile and is zero at the edge of contact and maximum at the initial or center point of contact. The maximum normal stress of the cylindrical contact is of course on the surface at the center of contact and is also the maximum contact pressure given by

$$p_{\max} = \frac{2F}{\pi bL} \tag{3.5}$$

However, the stresses that are recognized to cause yielding, the shear stress and von Mises stresses, are often maximum below the surface, as will be discussed next.

2.2 Elastic–Plastic Cylindrical Contact

If the force applied to a cylindrical contact increases enough, eventually the material will fail or yield. This usually occurs below the surface, because as mentioned previously, the maximum shear and von Mises stress are sometimes located not on the contacting surfaces but at a depth below them. Green [7] provides the following curve-fitted equations for the prediction of the initial yield or critical point for cylindrical contact according to the von Mises yield criteria. For the case of plane strain, the critical contact force to cause yielding is

$$\frac{F_c}{L} = \frac{\pi R\left(CS_y\right)^2}{E'} \tag{3.6}$$

where C is a piecewise equation given by

$$\begin{aligned} C &= \frac{1}{\sqrt{1 + 4(v-1)v}} \quad \text{when} \quad v \leq 0.1938 \\ C &= 1.164 + 2.975v - 2.906v^2 \quad \text{when} \quad v \leq 0.1938 \end{aligned} \tag{3.7}$$

In addition, the critical deflection and contact width are given by

$$\begin{aligned} \delta_c &= R\left(\frac{CS_y}{E'}\right)^2\left[2\ln\left(\frac{2E'}{CS_y}\right) - 1\right] \\ b_c &= \frac{2RCS_y}{E'} \end{aligned} \tag{3.8}$$

Note that $v = 0.1938$ also indicates a threshold where when v is greater than this, the point of initial yielding occurs below the surface, and when it is less, the initial yielding occurs on the surface. In addition, the case of plane stress can also be predicted by simply setting $v = 0$.

Unfortunately, very little work has been performed on cylindrical contact once the critical force has been surpassed and significant plastic deformation occurs. Actually, the case of sliding cylindrical contact has been investigated using the finite element method, but not the case of pure normal loading in a thorough manner that can be easily applied [8].

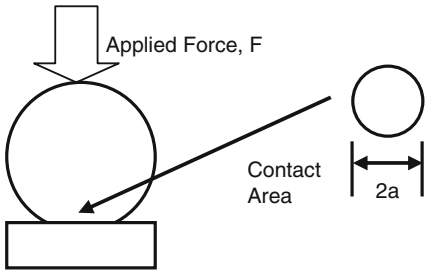

Fig. 3.3 Schematic of the contact area between a sphere and a flat surface

2.3 Elastic Spherical and Parabolic Contact

Similar to cylindrical or line contact, Hertz also solved the case of an axisymmetric parabolic contact, which is often used to model spherical elastic contact (see Fig. 3.3). Since a sphere initially contacts a surface only at a single point, this case is sometimes also referred to as point contact. This is also probably the most widely used contact model employed to describe single asperity contact occurring between two rough surfaces, as will be discussed later. This widely used model provides the contact force as a function of interference or deflection as

$$F = \frac{4}{3}E'\sqrt{R}(\omega)^{3/2} \tag{3.9}$$

And the contact area, which is circular, is given as

$$A = \pi R\omega = \pi a^2 \tag{3.10}$$

Note that E' and R are calculated using the same methodology outlined for cylindrical contact. It should also be noted that the maximum shear stress and von Mises stress occurs below the center of the contact area. Figure 3.4 shows the von Mises stress in a spherical contact as predicted by ANSYS™ finite element software. As will be characterized next, this causes initial yielding to occur below the surface. Similarly, surface fatigue can also initiate below the surface and allow cracks to propagate to the surface and cause large wear particles to detach and leave deep pits on the surface (i.e., pitting).

2.4 Elastic–Plastic Spherical Contact

Just as with cylindrical contact, when the contact force reaches a critical value, the stress state will start to cause yielding within the sphere. There are many models that have been devised to account for the plastic deformation in the sphere. Most models also assume that the deformation is elastic-perfectly plastic, meaning there

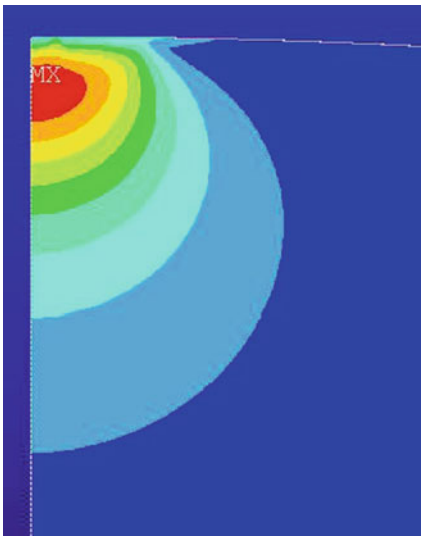

Fig. 3.4 The finite element predicted von Mises stress distribution in a spherical contact in the elastic regime ($\omega^* = 0.571$)

is no hardening in the material. However, there is no known analytical solution to this problem, and therefore, many previous models did not give the correct quantitative predictions, such as the groundbreaking model by Chang, Etsion, and Bogy (CEB) [9] and the work by Zhao, Maletta, and Chang [10] which attempted to improve on the CEB model by using a continuous template to bridge between the elastic and plastic regimes of deformation. Later, Kogut and Etsion [11] and Jackson and Green [12] improved upon these models by using the finite element method. Jackson and Green found the following equations for the prediction of initial yielding in the sphere according to the von Mises yield criteria [12]:

$$\omega_c = \left(\frac{\pi \cdot C \cdot S_y}{2E'}\right)^2 R \tag{3.11}$$

$$C = 1.295\exp(0.736\nu) \tag{3.12}$$

$$A_c = \pi^3 \left(\frac{CS_y R}{2E'}\right)^2 \tag{3.13}$$

$$P_c = \frac{4}{3}\left(\frac{R}{E'}\right)^2 \left(\frac{C}{2}\pi \cdot S_y\right)^3 \tag{3.14}$$

We can then normalize the area, contact force, and displacement by these critical values as

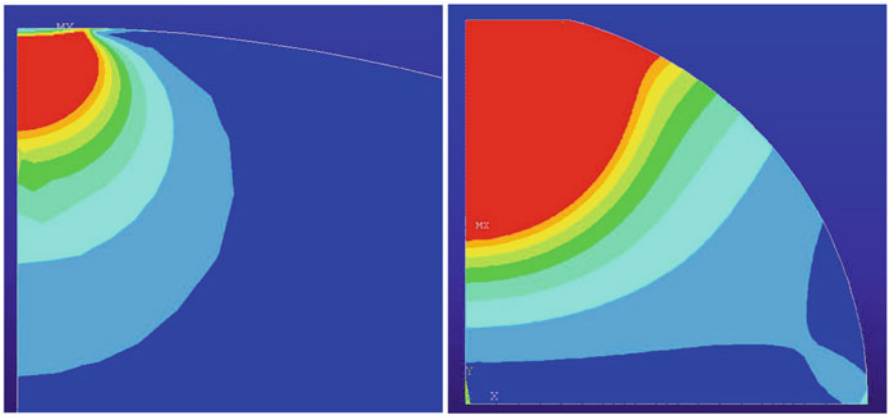

Fig. 3.5 The finite element predicted von Mises stress distributions for two interferences

$$A^* = A/A_c, \quad F^* = F/F_c, \quad \omega^* = \omega/\omega_c$$

Once yielding occurs, the volume of plastically deforming material spreads and surrounds an "island" of material near the center of contact that is under hydrostatic stress and therefore not yet yielded according to von Mises stress criteria (see Fig. 3.5). However, as the contact force is increased, eventually the entire surface in contact yields. When this occurs, it is usually referred to as fully plastic contact. Jackson and Green [12] found that the plastic deformation had a negligible effect on the contact until approximately $\omega^* = 1.9\omega_c$, which is now labeled as ω_t^*. According to the finite element-based empirical model by Jackson and Green, when the contact is effectively elastic ($0 \leq \omega^* \leq \omega_t^*$) the normalized contact force and area from Hertz contact simplify to

$$F^* = (\omega^*)^{3/2} \tag{3.15}$$

$$A^* = \omega^* \tag{3.16}$$

and once plastic deformation becomes more influential at $\omega_t^* \leq \omega^*$

$$F^* = \left[\exp\left(-\frac{1}{4}(\omega^*)^{\frac{5}{12}}\right)\right](\omega^*)^{3/2} + \frac{4H}{CS_y}\left[1 - \exp\left(-\frac{1}{25}(\omega^*)^{\frac{5}{9}}\right)\right]\omega^* \tag{3.17}$$

and the contact area is then

$$A_F^* = \omega^*\left(\frac{\omega^*}{\omega_t^*}\right)^B \tag{3.18}$$

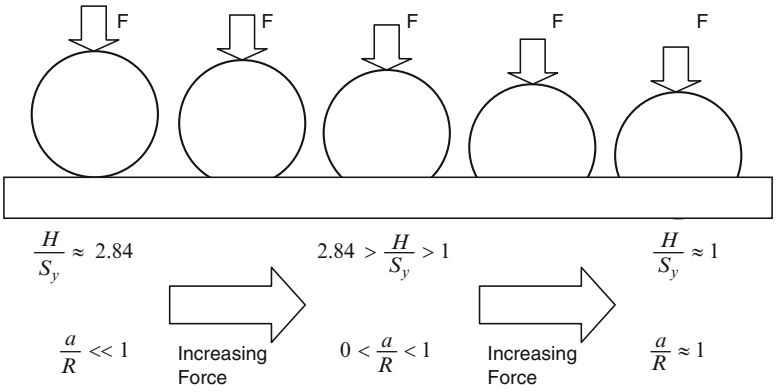

Fig. 3.6 Schematic showing how the pressure changes with the deformation of the sphere during fully plastic contact

$$B = 0.14\exp\left(23 \cdot \frac{S_y}{E'}\right) \tag{3.19}$$

where H is the effective fully plastic contact pressure, sometimes referred to as the hardness, which is given in updated form as

$$\frac{H}{S_y} = 2.84 - 0.92\left(1 - \cos\left(\pi\frac{a}{R}\right)\right) \tag{3.20}$$

Equation (3.20) captures the effect that large deformations of the sphere have on the contact pressure. As the sphere deforms, it changes from the shape of a curved contact toward a cylinder in contact with a flat (see Fig. 3.6). As this transition occurs, the average pressure for fully plastic contact changes from a value of approximately $2.8{\cdot}S_y$, as found by Tabor [2], to S_y.

Note that the Jackson and Green [12] equations are only valid up to $a/R = 0.41$. However, recently, Wadwalkar et al. [13] used finite elements to find a model that is valid for much larger loads and deformations until the contact radius nearly equals the radius of the sphere. Note that in these cases of severe deformation, the sphere actually begins to behave similarly to a barreling cylinder in compression. Additional studies have also considered how the sphere rebounds and what the residual stresses are once the sphere is unloaded [14, 15].

As mentioned previously, Kogut and Etsion [11] also developed their own empirical finite element model prior to Jackson and Green [12]. The model by Kogut and Etsion is much more simple than the Jackson and Green model and might be useful for a complex systems of equations. Even though the models do agree in some ranges [16, 17], it must be emphasized that the model is limited to small values of a/R and low interferences. In addition, the solution is piecewise and noncontinuous at the boundaries. Using the same normalization scheme, the Kogut and Etsion [11] model is given as follows:

When

$$1 \leq \omega^* \leq 6 \tag{3.21a}$$
$$A_{KE}^* = 0.93(\omega^*)^{1.136}$$
$$P_{KE}^* = 1.03(\omega^*)^{1.425}$$

When

$$6 \leq \omega^* \leq 110$$
$$A_{KE}^* = 0.94(\omega^*)^{1.146}$$
$$P_{KE}^* = 1.40(\omega^*)^{1.263} \tag{3.21b}$$

2.5 Spherical Indentation

In the elastic regime and at relatively small displacements, the contact of an elastic–plastic sphere against a rigid flat (i.e., flattening) and the contact of a rigid sphere against an elastic–plastic surface (i.e., indentation) are practically equivalent. However, as the displacements increase, the two cases begin to diverge [17]. Kogut and Komvopoulos [18] investigated elastic–plastic indentation and found a similar behavior of the fully plastic pressure to that of Jackson and Green [12]. This case is important for using indentation tests for the measurement of material properties. Kogut and Komvopoulos [18] found that the pressure during elastic–plastic indentation reached a maximum value that is less than the popular value of 2.84·Sy as a function of E'/S_y:

$$\frac{H}{S_y} = 0.201\ln\left(\frac{E'}{S_y}\right) + 1.685 \tag{3.22}$$

which is analogous to (3.20) for spherical flattening, rather than indentation, although in terms of the material properties rather than the deformed geometry. Additional equations are provided in [18] relating contact area and pressure to the penetration depth, and readers are advised to obtain the paper for additional information.

2.6 Elastic 2-D Sinusoidal or Harmonic Wavy Surface

Westergaard [19] first solved the case of perfectly elastic two-dimensional sinusoidal contact. From Westergaard's work, p^* is defined as the average pressure that when applied to the surfaces yields complete contact (i.e., no gaps between the surfaces). The average pressure required to obtain complete contact between the surfaces can be calculated as

$$p^*_{2D,elastic} = \pi E' \Delta/\lambda \tag{3.23}$$

Then, the contact area is related to the nominal pressure, $\overline{p}$ (including the regions out of contact), by

$$A = \lambda L(2/\pi) \sin^{-1}(\overline{p}/p^*)^{1/2} \tag{3.24}$$

Note that the contact area of the 2-D wavy surface is rectangular, similar to cylindrical contact, and might also be referred to as a "line" contact.

2.7 Elastic 3-D Sinusoidal or Harmonic Wavy Surface

Johnson et al. [20] characterized the contact of 3-D sinusoidal or harmonic surfaces. They found that no closed form analytical solution appears to exist over all ranges of deformation. First, they found that the average pressure to achieve complete contact for 3-D sinusoidal surfaces differs from the 2-D case and is

$$p^*_{3D,elastic} = \sqrt{2}\pi E' \Delta/\lambda \tag{3.25}$$

Then, using Hertz contact, they find the asymptotic solution to 3-D sinusoidal contact at low loads is

$$(A_{JGH})_1 = \frac{\pi}{f^2}\left[\frac{3}{8\pi}\frac{\overline{p}}{p^*}\right]^{2/3} \tag{3.26}$$

At high loads and when nearly all of the surfaces are in contact, Johnson et al. [20] found that the contact area is

$$(A_{JGH})_2 = \frac{1}{f^2}\left(1 - \frac{3}{2\pi}\left[1 - \frac{\overline{p}}{p^*}\right]\right) \tag{3.27}$$

Later, Jackson and Streator [21] fit an equation to these two asymptotic solutions that also appeared to agree with the numerical data in Johnson et al. [20]. This fit is given by

$$\begin{aligned} &\text{For} \quad \frac{\overline{p}}{p^*} < 0.8 \quad A = (A_{JGH})_1\left(1 - \left[\frac{\overline{p}}{p^*}\right]^{1.51}\right) + (A_{JGH})_2\left(\frac{\overline{p}}{p^*}\right)^{1.04} \\ &\text{For} \quad \frac{\overline{p}}{p^*} > 0.8 \quad A = (A_{JGH})_2 \end{aligned} \tag{3.28}$$

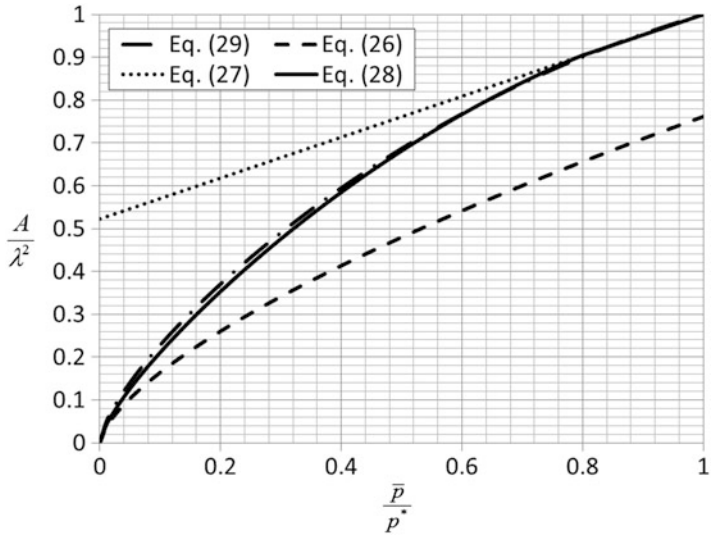

Fig. 3.7 The predicted contact area during sinusoidal contact as a function of average pressure

However, it was also later suggested that this equation could be approximated by the much more simple version here [22]:

$$\frac{A}{\lambda^2} = \left(\frac{\overline{p}}{p^*}\right) \wedge \left(\frac{2}{3} - \frac{\overline{p}}{4p^*}\right) \tag{3.29}$$

As shown in Fig. 3.7, (3.28) and (3.29) appear to agree well within most ranges of pressure and differ by an average error of approximately 2.7 %. However, at low pressures, (3.29) differs significantly from (3.28) by 30 % or more. Note that at very low pressures, Hertz contact can be assumed and that (3.29) does not asymptotically approach Hertz contact given by (3.26). Therefore, (3.29) does not appear to be a good approximation at low pressures and has errors above 5 % at approximately $\frac{\overline{p}}{p^*} < 0.2$.

2.8 Elasto-Plastic 3-D Sinusoidal Contact

Just as with spherical and cylindrical contact, as the contact force and pressure continues to increase, eventually it will cause yielding. If yielding initially occurs when only the tips of the sinusoidal surface are in contact, then it can still be modeled by spherical contact. Adapting the same critical equations derived for spherical contact for sinusoidal contact, the critical load and area are given by

$$F_c = \frac{1}{6\pi}\left(\frac{1}{\Delta f^2 E'}\right)^2 \left(\frac{C}{2}\cdot S_y\right)^3 \tag{3.30}$$

$$A_c = \frac{2}{\pi}\left(\frac{CS_y}{8\Delta f^2 E'}\right)^2 \tag{3.31}$$

where C is given as by (3.12). At low loads, $F < F_c$, and consequently small areas of contact, it is acceptable to assume that any deformation of the asperities in contact will behave perfectly elastically. However, as load increases to the critical value, plastic deformation will initiate within the asperities. Using the finite element method, Krithivasan and Jackson [23] developed empirical equations describing contacting sinusoidal surfaces by adapting existing spherical and elastic sinusoidal models:

$$A = (A_p)\left(1 - \left[\frac{\overline{p}}{p_p^*}\right]^{1.51}\right) + (A_{JGH})_2\left(\frac{\overline{p}}{p_p^*}\right)^{1.04} \tag{3.32}$$

where

$$A_P = 2\left(\frac{A_c}{2}\right)^{\frac{1}{1+d}}\left(\frac{3\cdot\overline{p}}{4CS_y}\lambda^2\right)^{\frac{d}{1+d}} \tag{3.33}$$

$$d = 3.8\cdot\left(\frac{E'}{S_y}\cdot\frac{\Delta}{\lambda}\right)^{0.11} \tag{3.34}$$

and p_p^* is the average pressure required to obtain complete contact between 3-D sinusoidal surface and a rigid flat according to the analysis by Jackson et al. [24], giving

$$\frac{p_p^*}{p^*} = \left(\frac{11}{4\cdot{}^{\Delta}/_{\Delta c} + 7}\right)^{3/5} \tag{3.35}$$

Jackson et al. [24] also analytically derive from the stresses for complete contact between sinusoidal surfaces, and according to the von Mises yield criteria, that the surface will deform elastically if its amplitude, Δ, is less than

$$\Delta c = \frac{\sqrt{2}\cdot S_y \exp\left(\frac{2v}{3}\right)}{3\pi E' f} \tag{3.36}$$

Likewise, when $\Delta > \Delta_c$, the surfaces deform elastic-plastically. It is very interesting to observe that the exact analytically derived (3.36) is very similar in form to (3.11) and (3.12) which were fit to a numerical solution. This gives greater confidence in those fits. Equation (3.35) predicts that the average pressure during heavily loaded contact can be much larger than the hardness, or three times S_y. This is due to the stress in sinusoidal contact becoming hydrostatic as complete contact

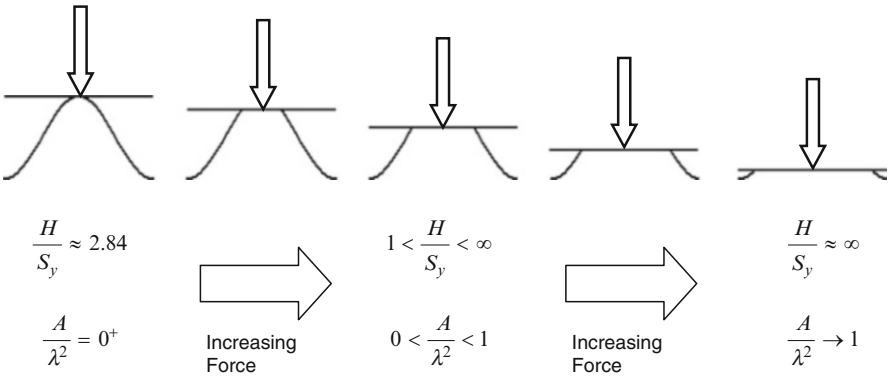

Fig. 3.8 The pressure change in the plastically deformed contact of sinusoidal surfaces

is approached. As shown in Fig. 3.8, this is in contrast to that predicted during spherical contact. In fact, the behavior is reversed. In elastic–plastic sinusoidal contact, the pressure can become much larger than yield strength as the contact area increases, while in spherical contact the contact pressure actually decreases toward a value of yield strength multiplied by unity.

2.9 *Impact of Spheres*

The impact of surfaces is very important for a wide variety of circumstances. For instance, it can be used to consider interactions in particulate flow, the performance of a particle damper, or perhaps even the impact of a bearing element against a raceway. Using (3.9), (3.10), (3.11), (3.12), (3.13), (3.14), (3.15), (3.16), (3.17), (3.18), (3.19), and (3.20), one can predict the energy lost in the impact of spheres due to elastic–plastic deformations. Here, we define V_1^* as the normalized velocity at the instant just before impact: $\left((V_1)^* = \frac{V_1}{V_c} \text{ and } V_c, = \sqrt{\frac{4\omega_c P_c}{5m}}\right)$. Using two different methodologies to describe the rebound of the spheres [14, 15] results in two sets of equations that both appeared to compare well with experimental data. First, when the elastic recovery predictions in Jackson et al. [14] are used, the following is obtained:

For $0 < V_1^* < 1$

$$e = 1 \tag{3.37}$$

For $1 < V_1^* \leq 60$

$$e = 1 - 0.1\ln\left(V_1^*\right)\left(\frac{V_1^* - 1}{59}\right)^{0.156}$$

For $60 \leq (V_1)^* \leq 1{,}000$

$$e = 1 - 0.1\ln(60) - 0.11\ln\left(\frac{V_1^*}{60}\right)\left(V_1^* - 60\right)^{2.36S_y/E'}$$

These equations combine to create a continuous prediction of e in the range of $0 < V_1{}^* < 1{,}000$. When the results of Etsion et al. [15] are used to predict the residual interference in the sequence to predict e, a good fit results from the following equation:

For $1 < (V_1)^*$

$$e = 1 - 0.0361\left(S_y/E'\right)^{-.114}\ln\left(V_1^*\right)\left(V_1^* - 1\right)^{9.5\varepsilon_y} \tag{3.38}$$

These equations may not be valid outside the ranges considered in deriving them ($0.0005 < S_y/E' < 0.01$ and $0.2 < \nu < 0.45$). The effect of strain hardening was also recently considered by Chaise et al. [25], who also confirmed the equations above for the impact of elastic-perfectly plastic materials

2.10 Adhesion Between Single Peaks

Under some conditions, such as when surfaces are contaminated, very rough, or relatively rigid, the effect of adhesion is negligible. However, for many other cases when the surfaces are very clean, smooth, and relatively soft, adhesion can play a very important role. Adhesion is simply the ability of surfaces in contact to maintain a tensile pressure before being pulled apart. Small quantities of water or fluid can also cause adhesion by forming a meniscus between the surfaces.

Surfaces in close vicinity tend to attract one another resulting in an adhesive force. Various sources can originate adhesion such as chemical bonds and physical forces. Examples of such sources for chemical bonds are ionic and covalent bonds and for physical forces are van der Waals and meniscus forces. Adhesion should be differentiated from cohesion when two identical materials bond together to form a new single material. Cohesion is measured when a material is broken into two different parts whereas if two surfaces (even made of the same material) are brought together, the force acting in between is called adhesion. The adhesion force, like the friction force, depends on the externally applied normal force. However, unlike the friction force, the adhesion exists even when there is no applied normal force on the surface. The force required to separate two adhered surfaces by the force of adhesion is called the "pull off force."

Adhesion happens in the interface of almost all materials and states of matter. A common example of the effect of adhesive forces between liquids and solids is the shape of a droplet on a surface. When the liquid/solid adhesive force is greater than the cohesive force of the liquid, the droplet tends to spread on the surface, such

as with water on glass. Whereas in the case of high liquid cohesion, droplet keeps a spherical form on the surface and minimizes the solid/liquid interfacial area, such as with oil on glass.

Molecules and atoms on the surface are the source of the adhesion. Therefore, contaminants, adsorbents, and thin films on the surface impose a great impact on the adhesive properties of a surface. Contaminants and adsorbents can dramatically reduce the adhesion of a surface. The existence of a liquid film can also result in the formation of a meniscus and affect the adhesion. Surface roughness decreases the real area of contact, and therefore, rougher surfaces tend to have less adhesion. Low stiffness, high normal load, creep, and other parameters that increase the real area of contact will also promote adhesion. Temperature changes the energy level of interfacial bonds and also the elasticity of the material which in turn can change the adhesion characteristics of the surface.

Generally, adhesion of a surface depends on many chemical and physical aspects of the surface and material which makes it difficult to calculate and characterize. Parameters such as work of adhesion, surface free energy, and interfacial energy are often used to avoid the complications of adhesion models [26]. The work of adhesion (W_{12}) is the energy change per unit area required to separate two surfaces (surface 1 and surface 2) from contact to separation by an infinite distance in a vacuum. The work of adhesion for two identical surfaces (W_{11}) is called the work of cohesion. The work of adhesion always has a positive value as the surfaces are attracted to one another in the vacuum. Surface energy (γ_1) is the energy required to increase the interfacial area of a media by a unit area. For liquids, γ_L is usually given in force per unit length (which is of the same dimension as energy per area) and referred to as surface tension. The surface energy of two immiscible liquids is called the interfacial energy (γ_{12}). Relations between these parameters are given in (3.39):

$$\begin{aligned} W_{12} &= \gamma_1 + \gamma_2 - \gamma_{12} \\ \gamma_{11} &= {}^{W_{11}}/_{2} \end{aligned} \tag{3.39}$$

In small-scale geometries where the surface to volume ratio increases, adhesion is an important and may be a dominant force. The domination of adhesion at the small scale was cited as one source of the contradictions observed between the Hertz contact model and experiments in the early of 1970s [27]. The first attempt to model adhesion between rigid spheres was carried out by Bradley [28], and the pull off force was calculated. Since Bradley, many models have been developed for spherical single asperity contact under certain assumptions. Johnson, Kendall, and Roberts (JKR) [27] developed a contact model assuming the adhesive force inside the contact area. Based on JKR, the radius of contact (a) when two spheres (R_1, R_2) with the elastic modulus, E, are compressed together under the applied load, F, is given by

$$a^3 = \frac{R}{E}\left[F + 3\pi R W_{12} + \sqrt{6\pi R W_{12} F + (3\pi R W_{12})^2}\right] \tag{3.40}$$

where $R = R_1 R_2/(R_1 + R_2)$. Note that this equation predicts an area of contact for the case even when no load is applied. The JKR model also predicts a pull off force of $F_s = -3\pi R W_{12}/2$, meaning that when the applied force equals to F_s, the two surfaces suddenly jump out of contact.

Assuming the Hertz contact solution inside the contact region and the adhesive force outside the contact area, Derjaguin, Muller, and Toporov [29, 30] developed an adhesion model also known as the DMT model. Equation (3.41) presents the radius of contact and pull off force according to this model:

$$\begin{aligned} a^3 &= \frac{3R}{4E}(F + 2\pi R W_{12}) \\ F_s &= -2\pi R W_{12} \end{aligned} \tag{3.41}$$

For a while it was thought that the DMT and JKR model are contradicting one another until Tabor [31] shed light on the matter by proving the fact that the two models are the limiting cases characterized by the Tabor parameter. Maugis [32] and Carpick-Ogletree-Salmeron [33] bridge the gap between the two models by introducing new assumptions and fitting equations.

Adhesion between rough surfaces can also be characterized using single asperity models and approaches such as statistical or multiscale methods. Fuller and Tabor [34] provided an adhesion parameter, θ_a, that qualitatively predicts the importance of adhesion in rough surface contact and is given by

$$\theta_a = \frac{E' \sigma_s}{W_{12}} \left(\frac{\sigma_s}{R}\right)^{1/2} \tag{3.42}$$

where σ_s is the RMS roughness of the asperity heights which will be defined later in Sect. 3.2 when discussing statistical rough surface contact models. When θ_a is greater than 10, adhesion is usually considered to be negligible in the contact of rough surfaces. In conclusion, adhesion can act as a helpful (a gecko walking on the wall) or a destructive mechanism (micron-sized devices stuck together). Therefore, careful study and understanding of it is of great importance in the area of contact mechanics.

2.11 Layered or Coated Single Peak Contacts

The ability to estimate the contact between a sphere and a thin-layered or thin-coated foundation is practically of great interest since thin coatings are widely used in industry. We will introduce the extended Hertz theory for circular point contact of coated bodies developed by Liu et al. [35] in this section, but many other cases of contact between layered surfaces are available in the literature. Liu et al. [35] provide a model of this contact problem by modifying the Hertz contact theory using a numerical analysis. As shown in Fig. 3.9, there is a coated layer on

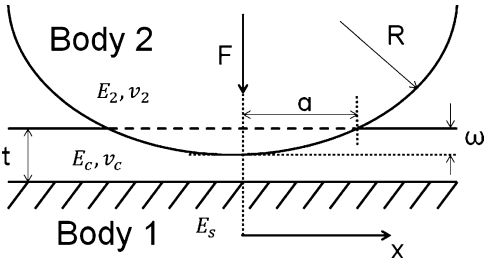

Fig. 3.9 Contact between a sphere and coated surface

body 1, which is considered the substrate, and body 2 is the elastic sphere. In this work the substrate (body 1) will be considered rigid ($E_s = \infty$).

The original Hertz solution is modified by using an equivalent elastic modulus (E^*) resulting in

$$\mathrm{F} = \sqrt{\frac{16\omega^3 E^{*2}}{9}} \tag{3.43}$$

$$a = \sqrt[3]{\frac{3FR}{4E^*}} \tag{3.44}$$

$$\frac{1}{E^*} = \frac{1}{E_1^*} + \frac{\left(1 - v_2^2\right)}{E_2} \tag{3.45}$$

where ω is the contact approach or interference, a is the contact radius, t is the thickness of the coating, F is the externally applied force, and R is the radius of the sphere. An externally applied force can be obtained using (3.43), and the contact radius and area is predicted by (3.44). The following procedure should then be followed. First, calculate the value of each necessary parameter (λ, κ, E_c^*, and H) using (3.47), (3.48), (3.49), and (3.50). The subscripts "c," "1," and "2" stand for material properties of the coating, body 1, and body 2, respectively. Then, the equivalent elastic modulus of the layered surface is predicted by the fit equations from Liu et al. [35]:

$$E_1^* = E_c^* \frac{1 - \left(\lambda + \kappa + 4\kappa\alpha^2 H^2\right)\exp(-2\alpha H) + \lambda\kappa\exp(-4\alpha H)}{1 + 4\alpha H\kappa\exp(-2\alpha H) - \lambda\kappa\exp(-4\alpha H)} \tag{3.46}$$

$$\lambda = 4v_c - 3 \tag{3.47}$$

$$\kappa = {}^{1}/_{\lambda} \tag{3.48}$$

$$E_c^* = \frac{E_c}{1 - v_c^2} \tag{3.49}$$

$$\mathrm{H} = {}^{t}/_{a} \tag{3.50}$$

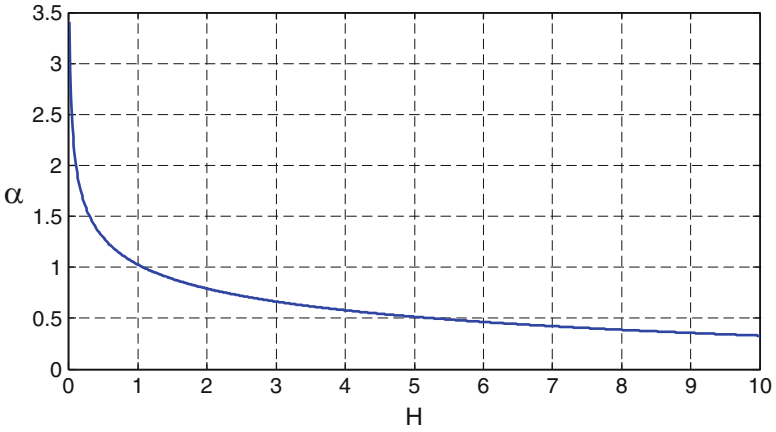

Fig. 3.10 Curve of α as a function of H

In order to find ω from a, use the Hertz contact theory (3.10). Next, obtain "α" from Fig. 3.10 with the H calculated above. Now, we can obtain E_1^* containing the overall characteristics of body 1 from (3.45) with the parameters we have calculated, and then, find E^* using (3.44). Finally, the applied force will be calculated using (3.43) with E^*. In this way, the applied force and resulting contact area on a circular point contact between a sphere and coated rigid substrate is obtained.

Liu et al. [35] also developed the ways to obtain applied force for the case of a circular point contact between a sphere and coated elastic substrate and an elliptical point contact. These other cases are omitted due to limited space but can easily be implemented from the original work.

An example of analysis for the contact between "aluminum" sphere and "glass" substrate coated with polydimethylsiloxane (PDMS) using the Liu et al. [35] model is presented next. The employed elastic modulus and Poisson's ratio of PDMS are approximately 615 kPa and 0.5, respectively. Also, the values of R and t are 5 and 1 mm, respectively. The relation between ω and a is determined by Hertz contact (3.10). To compare this model with the classical Hertz contact theory, the forces obtained by the Liu et al. [35] model and the Hertz contact theory are plotted in Fig. 3.11. The lines of "Hertz 1" and "Hertz 2" represent the contact forces in elastic spherical contact situations obtained by (3.9). "Hertz 1" is the prediction of the contact between an aluminum sphere ($E = 73.1$ GPa, $\nu = 0.35$) and a glass substrate ($E = 77.5$ GPa, $\nu = 0.2$) without a layer. "Hertz 2" is the prediction of the contact between an aluminum sphere and an infinitely thick PDMS layer. As expected, the layered model predicts forces between the two limiting cases.

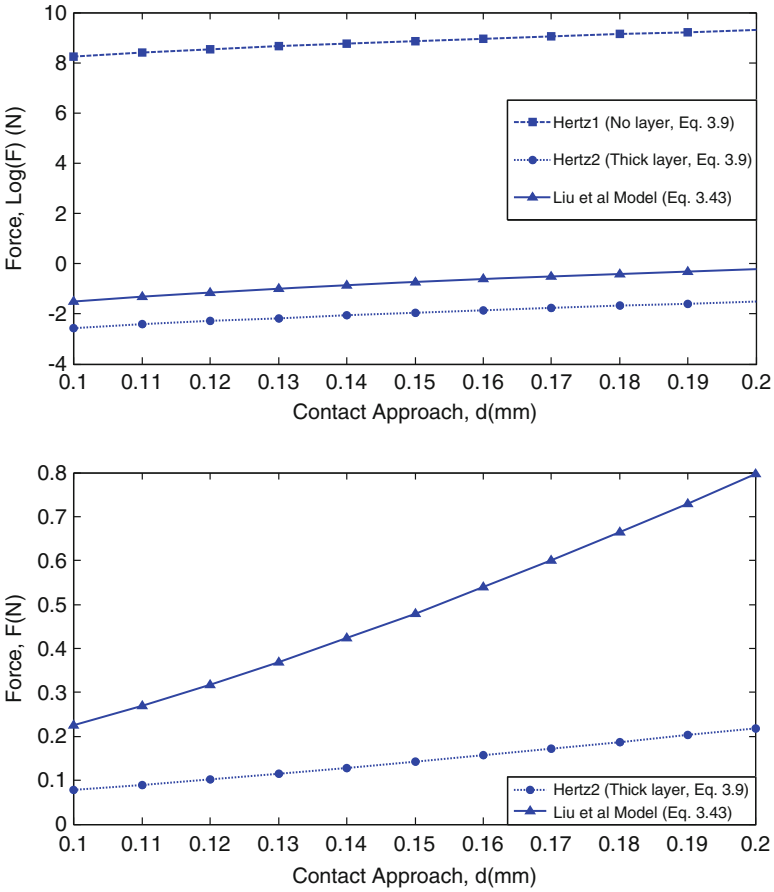

Fig. 3.11 Comparison of the layered contact model to the limiting Hertz contact cases

2.12 Creep in the Contact of Single Peaks

Creep is a time-dependent phenomenon which causes a change in the stress and strain in a material over time. In the contact between surfaces, creep causes a change in the contact area and contact pressure over time. Creep isn't an elastic behavior, and there is no recovered creep strain or reversible behavior under normal operating conditions, although elastic deformations are still recovered. Temperature and the presence of certain chemical solutions are environmental factors that may help some creeping materials to retrieve their initial shapes after a period of time. Any material may suffer from creep if certain conditions are met. It could be metals at high temperatures, polymers at room temperatures, and any material under the effect of nuclear radiation. There exists a variety of tribological applications that contact creep is of importance such as rail and wheel, MEMS RF switches, magnetic tapes, and also natural and artificial joints in the human body.

Different effects in contact between rough surfaces such as the rise in static friction due to dwell time and the rise in dynamic friction due to velocity and the friction lag and hysteresis can be described by the creep theory. The creep behavior depends on properties such as temperature and the stress level to which the material is exposed. Creep increases with temperature and is more dominant in materials that are exposed to heat for a long period of time.

For analyzing the creep behavior of materials, usually two approaches have been used in the literature. The first one is a classical approach [36] which is based on a combination of springs and dashpots, and the second approach uses empirical formulas which are based on experimental results to consider the effect of different creep parameters [37, 38]. In this text, the second approach is considered. Some of the empirical equations that have been used in creep modeling are listed as follows:

Power Law [39]

$$\dot{\varepsilon}_{cr} = C\sigma^n \tag{3.51}$$

Exponential Creep Law [39]

$$\dot{\varepsilon}_{cr} = C^{'}\exp(\beta\sigma) \tag{3.52}$$

Garofalo Law [40]

$$\dot{\varepsilon}_{cr} = C_1 \sinh^n(C_2\sigma) \tag{3.53}$$

Strain Hardening [39]

$$\dot{\varepsilon}_{cr} = C_1\sigma^{C_2}\varepsilon_{cr}^{C_3}e^{-C_4/T} \tag{3.54}$$

Modified Time Hardening [39]

$$\varepsilon_{cr} = \frac{C_1\sigma^{C_2}t^{C_3}e^{-C_4/T}}{(C_3+1)} \tag{3.55}$$

In the above equations, ε_{cr} is the creep component of the strain, σ is the nominal stress in the material, T is the temperature, and all the constants C, C', β, n, and C_i $(i = 1 - 4)$ are creep parameters which are obtained by curve fitting to the results of an accurate creep experiment.

It is suggested in [40] that the power creep law is only applicable to low stresses, but for high stresses, the exponential creep law gives better predictions. In addition, it is sometimes difficult to distinguish experimentally between the power and exponential creep laws. Therefore, the Garofalo creep law (3.53) was introduced which reduces to the power law for low stresses and to the exponential law for high stresses [40].

Only one case from two possible boundary conditions for analyzing creep will be considered in this chapter. Constant interference (i.e., relaxation) and constant load (i.e., creep) are the two possible cases, and only the first will be considered. Some models (i.e., [42] and [37]) assume constant normal force instead of constant displacement (i.e., [41]) for the contacting flat surface. The creep behavior of an elastic-perfectly plastic hemispherical asperity in fully plastic contact with a rigid flat surface, as analyzed by Goedecke and Mock [41], is discussed here. Fully plastic contact means that material has reached the yield stress everywhere in contact area.

We can write the following equation for the total strain tensor ε_{tot}, which can be separated into the creep, plastic, and elastic strain tensors:

$$\dot{\varepsilon}_{tot} = \dot{\varepsilon}_{cr} + \dot{\varepsilon}_{pl} + \dot{\varepsilon}_{el} \tag{3.56}$$

As the creep strain increases, the elastic strain, $\dot{\varepsilon}_{el}$, decreases, and the total stress reduces to $\sigma = C : \varepsilon_{el}$ with C being the elasticity tensor.[1] It is sufficient to formulate the uniaxial creep law, $\dot{\varepsilon}_{cr}(\sigma)$, where ε_{cr} and σ denote the equivalent strain and stress (von Mises stress), respectively. Using the Garofalo creep law with this model, as used in numerical simulations by Goedecke and Mock [41], two distinct phases of creep relaxation can be distinguished [37]. The asperity creeps with an accelerated creep rate in the first phase, but in the second phase, the asperity creeps with a much slower rate and no contact area change can be seen. It should be noted that the inclusion of a time- or temperature-dependent material creep law is straightforward as long as the hyperbolic sine dependence on stress is retained. In this case, the constant C_1 becomes a time- and temperature-dependent function $C_1(t,T)$ and can be included trivially in the equations describing the asperity behavior.

As mentioned before, in this model (Goedecke and Mock [41]) the contact between a hemispherical asperity and a rigid flat is under a fixed interference boundary condition δ (Fig. 3.12). It is assumed that $n = 1$ in the Garofalo formula (3.53) which corresponds to Persson's creep theory [43]:

$$\dot{\varepsilon}_{cr} = C_1 \sinh(C_2 \sigma) \tag{3.57}$$

The creep constant C_1 in the Garofalo formula shows the characteristic time scale in the creep process, and the results are presented with respect to this scaled time:

$$\tau = t/t_1 = t\frac{EC_1}{H} \tag{3.58}$$

[1] In this notation, the colon (:) marks a reduction of the full tensor grade by 2; i.e., a multiplication of a tensor of the fourth grade with a tensor of the second grade yields a tensor of second grade.

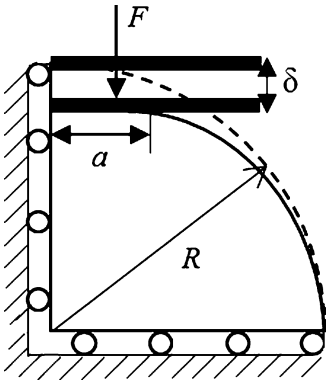

Fig. 3.12 A hemispherical asperity with radius R before and after loading, showing the contact radius a, the displacement δ, and the load F

In Fig. 3.13, the force F and the contact area A dependence on τ for reference parameters (set number 1 in Table 3.1) are shown. It can be seen that the contact area change flattens and it remains constant after an initial rise of about 7 %. The contact force, on the other hand, shows a steep initial reduction and a slowing creep rate as time increases.

The finite element simulations include two steps: (a) displacing the rigid flat to reach to a predefined interference δ as shown in Fig. 3.12 and (b) creep relaxation at this fixed interference. Jackson and Green [12] formulas can be used (see (3.11), (3.12), (3.13), (3.14), (3.15), (3.16), (3.17), (3.18), (3.19), and (3.20)) to obtain the state of the sphere before creep initiates (Step (a)). Using the Garofalo creep law (3.53) and considering the fact that the total strain is constant at ε_0 because of fixed interference boundary condition, the following equation can be obtained for the contact area as it changes in time due to creep:

$$A(t) \approx A_0 \left[1 - (1 - 2\nu) \left(\varepsilon_0 - \frac{2}{EC_2} \text{arctan}h(-C_1 C_2 t + \xi) \right) \right] \tag{3.59}$$

where A_0 is the initial contact area before creep starts and ξ is an integration constant. So a time evolution law for the change in contact area (ΔA) is

$$\frac{\Delta A(t, C_2, \delta)}{A_0} = \frac{\Delta A(C_2, \delta)}{A_0} [1 - 2c(p_1, p_2) \text{arctan}h\{\exp(-p_1 \tau(t) + p_2)\}] \tag{3.60}$$

where

$$c(p_1, p_2) = [2\text{arctan}h(\exp(p_2))]^{-1} \tag{3.61}$$

to set $\Delta A(t = 0) = 0$. p_1 and p_2 are the fit parameters, and their values for the example material properties listed in Table 3.1 are given as

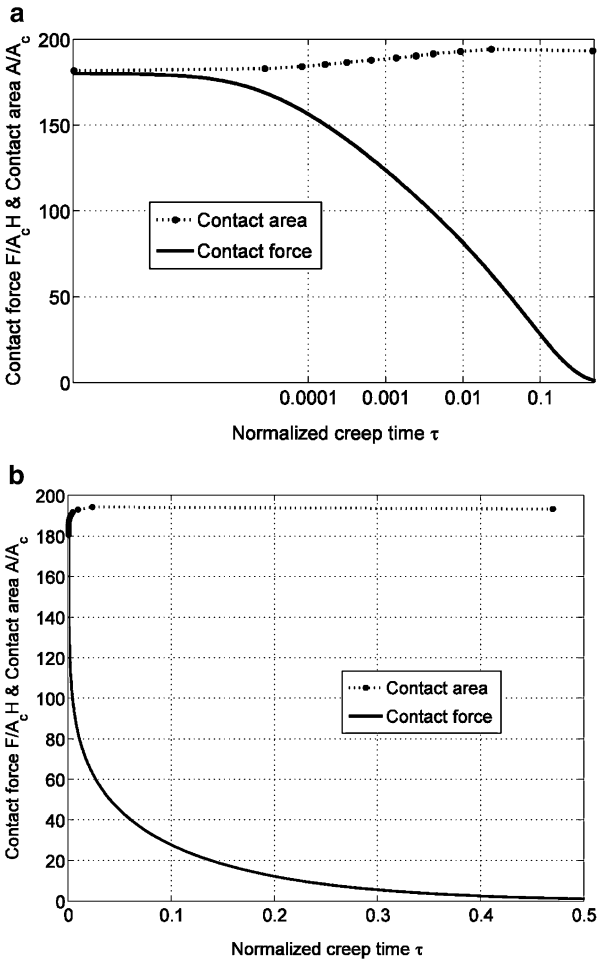

Fig. 3.13 Creep relaxation of force (*solid line*) and evolution of contact area (*dashed line*) with respect to normalized creep time in a logarithmic (**a**) and conventional (**b**) scale

Table 3.1 Overview of parameter ranges used for simulation [36]

Run no.	Varied parameter	Range
1	None (reference)	$R = 1mm$, $E = 200GPa$, $\upsilon = 0.33$ $\sigma_Y = 400MPa$, $(C_1 = 10^{-4}s^{-1})$ $C_2 = 10/\sigma_Y$, $\delta = 100\delta_c$
2	Radius R	$0.1 - 10mm$
3	Interference δ	$25\delta_c - 600\delta_c$
4	Poisson's ratio υ	$0.28 - 0.38$
5	Yield stress σ_Y	$200 - 2000MPa$
6	Young's modulus E	$70 - 300GPa$
7	MCL parameters C_1, C_2	$C_1 = 10^{-3} - 10^{-5}s^{-1}$, $C_2 = 5 - 15/\sigma_Y$

$$p_1 = 27 \pm 5$$

and

$$p_2 = -(1 \pm 0.4) \times 10^{-3} \tag{3.62}$$

The pressure rate or relaxation rate for the second step (b) is obtained from the following equation:

$$\dot{p}(p) = -\sum_{i=1}^{2} A_i \sinh(\alpha_i p) \tag{3.63}$$

The A_i and α_i are dependent on input parameters such as the fixed interference δ and the asperity radius R and are obtained by curve fitting to accurate numerical or experimental results. Extending (3.63),

$$-\dot{p} = A_1 \sinh(\alpha_1 p) + A_2 \sinh(\alpha_2 p) \tag{3.64}$$

where the constants A_i and α_i are obtained using the following empirical equations:

$$\begin{pmatrix} A_1 \\ A_2 \end{pmatrix} = EC_1 \left\{ \begin{pmatrix} 2.933 \pm 0.076 \\ -0.035 \pm 0.019 \end{pmatrix} + C_2 \sigma_Y \begin{pmatrix} 0.001 \pm 0.010 \\ 0.089 \pm 0.002 \end{pmatrix} \right\} \tag{3.65}$$

$$\begin{pmatrix} \alpha_1 \\ \alpha_2 \end{pmatrix} = \frac{1}{H} \left\{ \begin{pmatrix} 0.43 \pm 0.14 \\ 3.43 \pm 0.23 \end{pmatrix} + C_2 \sigma_Y \begin{pmatrix} 0.57 \pm 0.02 \\ 0.85 \pm 0.03 \end{pmatrix} \right\} \tag{3.66}$$

The second case that is considered here is creep under the constant force boundary condition as described by Brot et al. [38]. In reference [38], a polymeric biomaterial is used to model the single hemispherical asperity, and they also used a simplified form of the modified time hardening law (3.55) for their model because it better predicts the experimental results for polymers. Since biomaterials are used over a narrow range of temperatures, the temperature dependency can be ignored. Therefore, by substituting the simplified form of (3.55) into a sum of the different components of the strains, (3.56) gives

$$\varepsilon = \varepsilon_{elastic} + \varepsilon_{cr} = \frac{\sigma}{E} + \overline{C}_1 \sigma^{C_2} t^{C_3} \tag{3.67}$$

The above equation is called the simplified modified time hardening law (MTH) where E is the linear elastic modulus of the polymer and the parameter $\overline{C}_1$ is defined as

$$\overline{C}_1 = \frac{C_1}{(C_3 + 1)} \tag{3.68}$$

Brot et al. [38] found the following equations for the creep displacement and creep contact area using (3.67), and by performing a parametric analysis to study the effect of the various variables obtained the following

$$\omega_{cr}(t) = \omega_{cr}(t_r)\left(\frac{t}{t_r}\right)^{(0.71C_3+0.03)} \tag{3.69}$$

$$A_{cr}(t) = C_2\pi R\omega_{cr}(t_r)\left(\frac{t}{t_r}\right)^{(0.71C_3+0.03)} \tag{3.70}$$

In the above equations, $\omega_{cr}(t)$ and $A_{cr}(t)$ are the time-dependent creep displacement and creep contact area, respectively. It should be noted that $\omega_{cr}(t_r)$ is the creep displacement at a convenient reference time t_r, R is the radius of the hemispherical asperity, and C_2 and C_3 are constants that are calculated by curve fitting the equation to the experimental results. As shown by the equations, Brot et al. [38] found a linear relation between the area evolution $A_{cr}(t)$ and interference $\omega_{cr}(t)$.

2.13 Sliding and Tangentially Loaded Contacts

Ultimately, the goal of many of the contact models is to be able to predict friction and wear between sliding surfaces. Unfortunately, no theoretical model of friction or wear has been universally successful in making predictions based on the material properties, surface geometries, operating conditions, etc. Nonetheless, we will briefly introduce some of the concepts of sliding in contact mechanics here. Sliding is essentially the application of a tangential load to a contacting asperity. Many previous works have considered the effect of tangential load on the elastic contact between a contacting sphere and a flat, and we suggest you look to these prior works for more information [44–46]. The elastic–plastic contact of a sphere against a flat surface has also been studied since Chang et al. [47] were first interested in predicting the static friction between metallic surfaces. The concept is that two asperities will bond together on the surface, and that the bond must be yielded by the combined stresses induced by normal and tangential loading for sliding to occur. An anomaly of this theory is that for very highly loaded surfaces on which the contacts are yielded, no additional force is needed to induce sliding, and the friction is theoretically nil. More recently, Brizmer et al. [48] used a finite element analysis to predict the tangentional load, Q_{max}, required to break the contact or cause sliding between a sphere and a flat with a full stick condition initiated between the surfaces and provide an empirical fit as

$$\mu = \frac{Q_{\max}}{F_n} = 0.26\ \coth\left(0.27\left(\frac{\omega}{\omega_c}\right)^{0.46}\right) \tag{3.71}$$

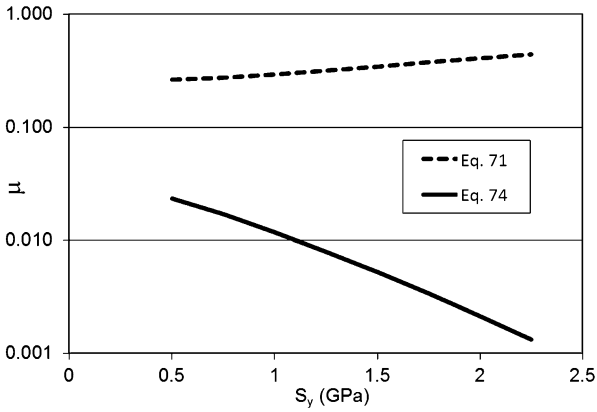

Fig. 3.14 Comparison of two elastic-plastic models of the tangential loading of spheres against a rigid flat (3.71) and against another identical sphere (3.74)

where F_n and ω are the normal preload and deflection before the tangential load is applied, respectively. Be careful to note that this is not the conventional friction coefficient, but the ratio of tangential to normal force for a single contact. Since (3.71) is intended to consider single asperity contact in order to predict friction between the surfaces, the full stick condition is intended to model the adhesive bonding or cold welding that can take place between asperities on surfaces and is believed to be one of the main sources of friction.

Alternatively, another finite element-based work characterized the lateral interaction of two spheres deforming in the elastic–plastic range [49]. This interaction might be considered the plowing or abrasive mechanism in friction and wear, as opposed to the adhesive mechanism. To isolate the plowing effect, the friction between the interacting spheres was set to zero. From an extensive finite element simulation, the following fit equations were found for average normal force, average tangential force, and single contact friction averaged over the entire interaction of the two spheres, respectively:

$$\frac{F_n}{P} = 0.59\left[\left(\frac{\delta}{\omega_c}\right)^{1/5}\left(1 - 0.656\left(\frac{1}{e_y}\right)^{1/20}\right)\left(\frac{\nu}{0.33}\right)^{1/10}\right] \tag{3.72}$$

$$\frac{F_t}{P} = 4.5 \cdot 10^{-7}\left[\ln\left(\frac{\delta}{\omega_c}\right)^{20/3}\left(113e_y\right)^2\left(\frac{\nu}{0.33}\right)^{2/3}\right] \tag{3.73}$$

$$\mu = \frac{F_t}{F_n} = 7.63 \cdot 10^{-7}\left[\ln\left(\frac{\delta}{\omega_c}\right)^{20/3}\left(\frac{\omega_c}{\delta}\right)^{1/5}\frac{\left(113e_y\right)^2}{1 - 0.656\left(e_y\right)^{-0.05}}\left(\frac{\nu}{0.33}\right)^{0.56}\right] \tag{3.74}$$

where e_y is S_y/E' and δ is the interference between the interacting spheres. Note that the fits are limited in applicability to $0.01 < \delta/R < 0.025$ and $1.66 \times 10^{-3} < e_y < 22.5 \times 10^{-3}$. Since the fits presented by (3.71), (3.72), (3.73), and (3.74) represent the source of friction from two different mechanisms, it is possible to qualitatively compare the proportion of friction from the two mechanisms as shown in Fig. 3.14. The results shown are for $E = 200$ GPa, $\nu = 0.33$, $\delta = \omega = 0.1$ μm, and

$R = 10$ μm, and the yield strength is varied as shown. These values could represent an asperity on a steel surface. The results of this comparison suggest that the adhesive source of friction is much larger than the plowing portion. However, it is possible that under certain conditions this might not be the case, for instance if the surfaces are lubricated. In addition, it appears that for very soft materials that the two curves would cross and reverse order. Then, it is also interesting to note that the two mechanisms appear to be affected by the yield strength in opposite ways. They may result in the effect of yield strength cancelling out. Another recent paper uses a semianalytical method to also consider rolling motion [50]. Even more recently, Mulvihill et al. [51] examined a similar case but included the effect of a shear strength at the contact bond between the surfaces.

3 Rough Surface Contact

3.1 Background

All surfaces, if looked at the proper magnification, show some roughness or deviation from being perfectly smooth. In some cases, this may mean considering the atomic scale of the surface where roughness is inherent due to the particle-based structure of matter. In contrast, some surfaces appear rough with no magnification at all. Regardless of what scale the roughness appears, it will cause contact between surfaces to begin at the peaks and difficult to accurately model. This roughness also usually does not only appear at one scale but over many scales (see Fig. 3.15). This results in the geometry of surfaces being very difficult to describe in detail.

Even though the roughness of surfaces is very difficult to describe, the contact between rough surfaces governs many phenomena in our world, such as friction, wear, thermal contact resistance, and electrical contact resistance. Therefore, it is extremely important to be able to at least make reasonable predictions of the pressure and real area of contact between two contacting rough surfaces. The real area of contact between surfaces defines what solid material actually comes into contact when two surfaces are pressed together. For example, if you asked most people what the area of contact was between this textbook and a table is, they would identify the rectangular profile of the book, which is commonly referred to as the nominal or apparent area of contact. However, what's actually in contact are only the peaks or asperities on the surfaces of the book and the table. This results in the pressures on these asperities being much higher than what is nominally applied to the book.

Archard [1] was probably the first to model contact between rough surfaces by the stacking of spheres of different sizes. He was the first to show that the real contact area is often nearly linearly proportional to the contact force. This was later confirmed by others such as Bush et al. [52] and Greenwood and Williamson [3] and has important implications in explaining Amonton's friction equation

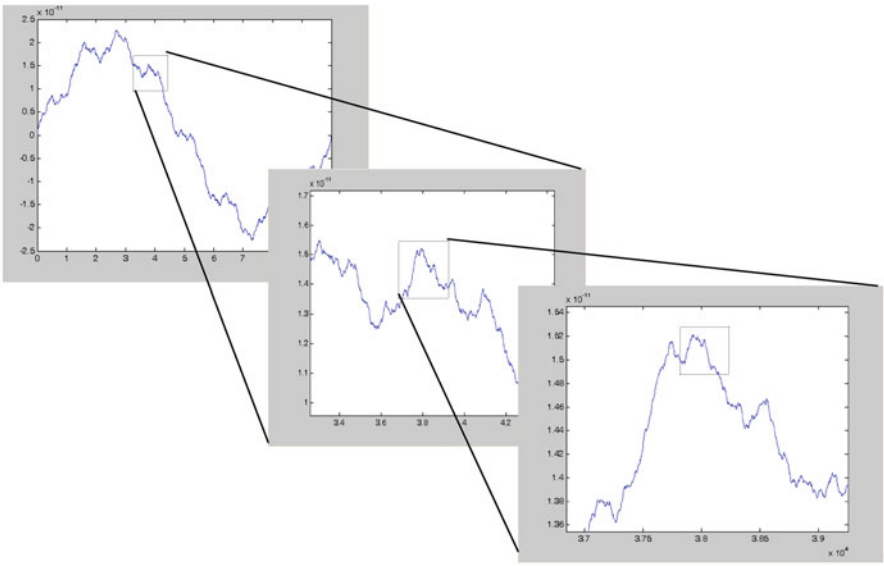

Fig. 3.15 Illustration of how surface roughness can appear at different magnifications and therefore at different scales

(i.e., friction is independent of nominal area and dependent on normal load). If the friction force is proportional to the real area of contact, then according to these models, Amonton's friction equation is explained.

In addition, it is extremely difficult, and perhaps even impossible, to measure the actual or real area of contact between many surfaces under practical conditions. This is because the individual asperity contact areas are not only often very small but hidden between the surfaces. Some researchers have had some success with acoustic [53], optical [54], electrical [55], and thermal measurements [56]. Nonetheless, it is difficult to verify the various rough surface contact models in the literature, and for these reasons, there are many of them. It would require another book to describe all rough surface contact models and is impractical to review them all here, but we will cover a few that we believe are the most practical and accurate.

If one attempts to consider the entire surface geometry, such as by meshing the entire surface and solving the contact and deformation using finite elements, then the method is considered to be deterministic. However, these models are not truly deterministic because it is currently practically impossible to adequately include all the detail of a rough surface. However, there are a few methods that have shown promise in this area. There are many methods that also seek to improve the computational efficiency via semianalytical approaches [57], multigrid methods, or by solving the problem in the frequency domain [58, 59]. Samples of a rough surface contact problem solved in the frequency domain using the method outlined by Stanley and Kato [59] are shown in Figs. 3.16, 3.17, and 3.18. For generality,

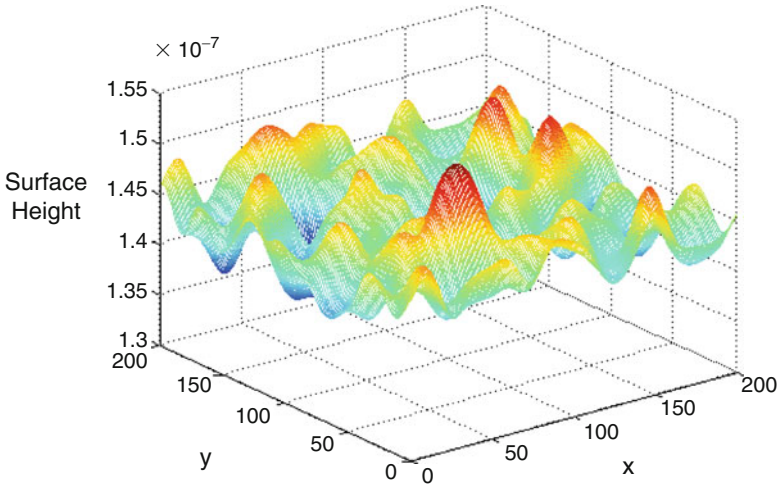

Fig. 3.16 A rough surface modeled using the FFT deterministic method for elastic contact (using Stanley and Kato [59])

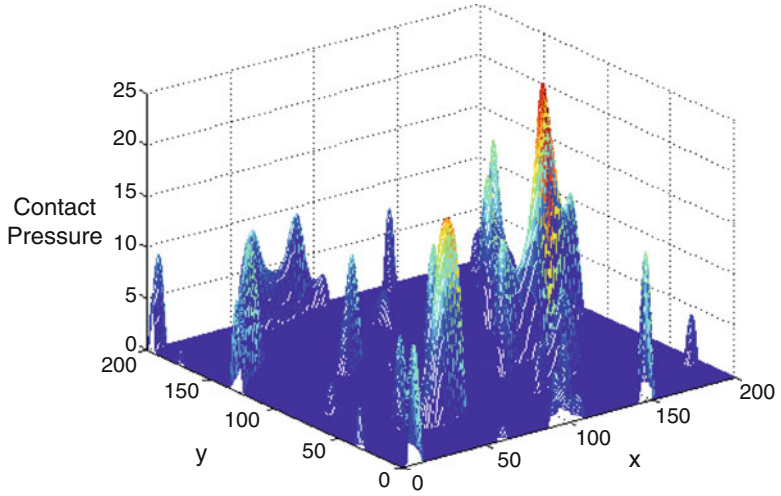

Fig. 3.17 The pressure distribution of the rough surface shown in Fig. 3.16 solved by using the FFT deterministic method for elastic contact

these figures are left without units. In Fig. 3.16, the initial geometry is shown. In Fig. 3.17, the contact pressure is shown, and finally, in Fig. 3.18, the deformed geometry of the surface is shown. It is easy to see in these figures how the peaks or asperities are only in contact and incur high pressures.

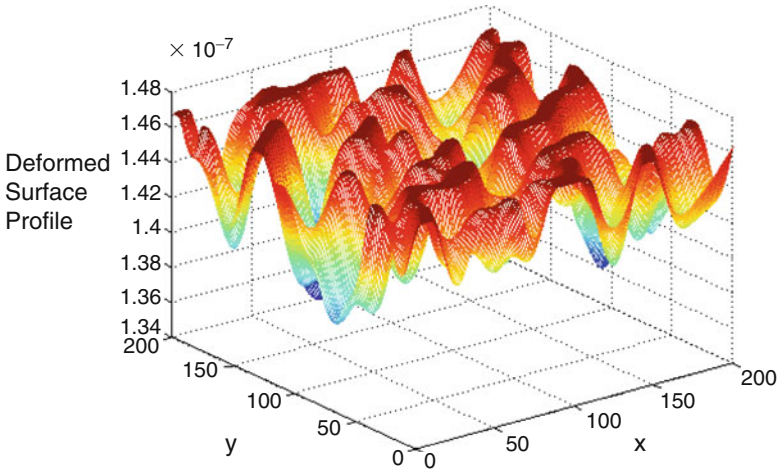

Fig. 3.18 The deformed profile of the rough surface shown in Fig. 3.16 solved by using the FFT deterministic method for elastic contact

Since deterministic methods are very computationally expensive, many methods have been developed by modeling the rough surface using different mathematical models. The main methods are here categorized by the implemented mathematical methodology as (1) statistical, (2) fractal, and (3) multiscale. Here, we will discuss only the statistical and multiscale models in detail. This is partly due to the fact that fractal-based models have been found to predict a nonphysical result: zero contact area. It should be emphasized that all rough surface contact models should be used with great care because they all make underlying assumptions about the surfaces that are in contact.

Since rough surfaces possess very complicated geometries and appear "random" in nature, it is logical to employ statistics to describe them. Greenwood and Williamsons' [3] seminal work first set the foundation for the statistical-based modeling of rough surface contact. In their work the height of a surface, z, is described by a Gaussian distribution as

$$\phi = (2\pi)^{-1/2}\left(\frac{\sigma}{\sigma_s}\right)\exp\left[-0.5\left(\frac{z}{\sigma_s}\right)^2\right] \tag{3.75}$$

where σ is the root mean squared (RMS) roughness of the surface, also commonly referred to as the standard deviation, and σ_s is the RMS roughness of just the peaks or asperities on the surface, since the asperities are what will come into contact when a rough surface is pressed against another surface. Now, consider that if one wishes to calculate the number of asperities that are taller than a height, d, one would solve the integral:

$$N(d) = \eta A_n \int_d^\infty \varphi(z)dz \tag{3.76}$$

Now, consider if an opposing surface was a distance, d, away from the rough surface. Then, the peaks that are above this height would actually be in contact with the opposing surface. Therefore, to predict the area of contact between the surfaces, one would sum the individual areas of each asperity. This can be accomplished with the statistical model using the equation below provided by Greenwood and Williamson [3]:

$$A(d) = \eta A_n \int_d^\infty \overline{A}(z-d)\phi(z)dz \tag{3.77}$$

Similarly, the total contact force can be calculated by

$$P(d) = \eta A_n \int_d^\infty \overline{P}(z-d)\phi(z)dz \tag{3.78}$$

but note that this model neglects the lateral interactions between asperities. In the original Greenwood and Williamson model, the radius of curvature for all of the asperities was assumed to be constant, but later, Bush et al. [52] and Whitehouse and Archard [60] alleviated that assumption. Nonetheless, for simplicity this assumption was still adopted by many subsequent works. The individual asperity contact areas, $\overline{A}$, and asperity force, $\overline{P}$, can be predicted by many of the models discussed earlier in this chapter (see (3.9), (3.10), (3.17), and (3.18)), and many works have examined the effects of various asperity models, height distributions, the effect of lateral asperity surface interaction, a deformable substrate, etc. [9, 61–70]. However, in the original work by Greenwood and Williamson [3], the asperities were assumed to always remain elastic so that Hertz contact could be used. For many years, the model was only used by numerically integrating the equations or simplifying the distribution. However, very recently an analytical solution was found and is given as [71]

$$\frac{P}{A_n E'} = \beta\left(\frac{\sigma}{R}\right)^{1/2} J_p \tag{3.79}$$

$$\frac{A_r}{A_n} = \pi\beta \cdot J_a \tag{3.80}$$

$$J_a = \sqrt{\frac{1}{2\pi}}\sigma_s^* e^{-\alpha^2/2} - \frac{d^*}{2} erfc\left(\frac{\alpha}{\sqrt{2}}\right) \tag{3.81}$$

for $d^* > 0$

$$J_p = \frac{\sigma_s^*}{4}\sqrt{\frac{d^*}{\pi}} e^{-\alpha^2/4}\left[\left(1+\alpha^2\right)K_{1/4}\left(-\alpha^2/4\right) - \alpha^2 K_{3/4}\left(-\alpha^2/4\right)\right]$$

for $d^* = 0$

$$J_p = \frac{\Gamma(5/4)}{\sqrt{\pi} 2^{1/4}} \left(\sigma_s^*\right)^{3/2}$$

for $d^* < 0$

$$J_p = \frac{^*_s}{4} \times \sqrt{\frac{d^*}{2}} e^{^2/4} \left[\left(1 + {}^2\right) I_{1/4}\left({}^2/4\right) + \left(3 + {}^2\right) I_{1/4}\left({}^2/4\right) + {}^2 \left(I_{3/4}\left({}^2/4\right) + I_{5/4}\left({}^2/4\right) \right) \right] \tag{3.82}$$

where $\Gamma(\cdot)$ is the Gamma function, $I(\cdot)$ and $K(\cdot)$ are the modified Bessel functions of the first and second kinds, respectively, and $erfc(\cdot)$ is the complementary error function. Also note that "*" denotes a length normalized by σ_s, and the equations use the definitions $\beta = \eta\sigma R$, $d^* = h^* - y_s^*$, and $\alpha = d^*/\sigma_s^*$. In order to practically implement the Greenwood and Williamson model and other statistically based rough surface contact models, one must obtain the statistical parameters for the contacting surfaces. McCool [72] provides a widely used spectral moment-based approach. First, the spectral moments are calculated by

$$m_2 = \frac{1}{N} \sum_{n=1}^{N} \left(\frac{dz}{dx} \right)_n^2 \tag{3.83}$$

$$m_4 = \frac{1}{N} \sum_{n=1}^{N} \left(\frac{d^2 z}{dx^2} \right)_n^2 \tag{3.84}$$

and m_0 is merely the mean squared roughness (σ^2). For discrete rough surface data, (3.83) and (3.84) can be calculated using the finite difference method. For two rough surfaces in contact, the spectral moment of each surface is added together to give the equivalent spectral moment used to calculate the statistical parameters. As an example, for two identical surfaces the spectral moments would merely be doubled. Then, the other required statistical quantities can be easily calculated as

$$\eta = \frac{m_4}{6\sqrt{3}\pi \cdot m_2} \tag{3.85}$$

$$R = 0.375 \cdot \left(\frac{\pi}{m_4} \right)^{0.5} \tag{3.86}$$

$$\sigma_s^2 = \sigma^2 - \frac{3.717 \cdot 10^{-4}}{\eta^2 R^2} \tag{3.87}$$

and from Front [73]

$$y_s = \frac{0.045944}{\eta R} \tag{3.88}$$

Greenwood and Williamson [3] also knew that the stresses in the asperities could be very high and therefore they are very likely deforming in the elastic–plastic range. To quantify the relative amount of the plastic deformation between contacting surfaces, they derived the dimensionless plasticity index given by

$$\psi = \sqrt{\frac{\sigma_s}{\omega_c}} \tag{3.89}$$

Recall that ω_c is the critical interference in spherical contact given by (3.11). One then uses the average radius of the asperities on the surface (3.86). The plasticity index can vary over several orders of magnitude. The meaning of ψ is qualitative, and higher values signify relatively more plastic deformation of the contacting asperities. Generally, it shows that plastic deformation increases with roughness and decreases with yield strength. Note that the amount of plastic deformation also depends on the force pressing the surfaces together. The transition from the elastic to elastic–plastic regime of rough surface contact is said to occur at approximately ψ=1. A similar prediction of the plasticity index was derived using the multiscale stacked asperity contact model that is discussed next. If a high plasticity index is calculated, it is recommended that a rough surface contact model that considers plastic deformation is used, such as by including the elastic–plastic asperity models in (3.17), (3.18), (3.19), (3.20), and (3.21) or by using the elastic–plastic multiscale models described next.

3.2 Multiscale-Based Models

Initiated from Archard's theory [1] many years ago, recently, the multiscale modeling technique has become more popular [21, 56, 74–79]. Archard suggested that the asperities of rough surfaces must be modeled as "protuberance upon protuberance." However, Archard first used spheres to model the scales of asperities or protuberances, which is difficult to relate to actual surfaces. To some extent, sinusoidal contact may be a more realistic depiction of surface asperity contact, especially at high loads, than spherical contact. A fairly recent multiscale rough surface contact model considering sinusoidal-shaped asperities is described here [21, 78, 79]. In this model, the different scales of asperities on a surface are characterized using a fast Fourier transform (FFT). Since the model needs an iterative numerical algorithm to solve, a simplified version of the model is then proposed which assumes that the real contact pressure is proportional to the maximum ratio of the amplitude to the wavelength for the surface acquired from FFT.

The full iterative version of the model also has the assumptions:

1. Asperities are arranged so that asperities of smaller cross-sectional surface area are located on top of larger asperities.
2. Each scale of asperities carries the same total load (i.e., the scales are in a mechanical series).
3. The load is divided equally among all the asperities at each scale (i.e., in mechanical parallel).
4. At each scale, the asperities deform according to a chosen contact model irrespectively of any smaller scales.

Using these assumptions and Archard's stacked asperity concept, the following equations are derived that predict the real area of contact:

$$A_r = \left(\prod_{i=1}^{i\max} \overline{A}_i \eta_i \right) A_n \tag{3.90}$$

$$F = \overline{F}_i \eta_i A_{i-1} \tag{3.91}$$

where A_r is the real area of contact, F is the contact load, and A_n is the nominal contact area. Parameters $\overline{A}_i$ and $\overline{F}_i$ are the single asperity contact area and single asperity contact force at a given scale level, respectively. The subscript i denotes a scale or frequency level and $i_{\max}$ denotes the highest frequency level considered. The area of contact at a given frequency level is denoted by A_i, and η_i is the corresponding areal asperity density. The parameters describing the surface topography (such as Δ and f) are calculated from an FFT performed of the surface profile. Then, the value of η is given by

$$\eta_i = 2f_i^2 \tag{3.92}$$

where f_i denotes the frequency (i.e., the reciprocal of wavelength).

The number of asperities at level I, N_i, is given by

$$N_i = \eta_i A_{i-1} \tag{3.93}$$

Hence, the load on each individual asperity at level I, $\overline{F}_i$, is given by (note that this is equivalent to (3.91))

$$\overline{F}_i = \frac{F}{N_i} \tag{3.94}$$

Using (3.94), one finds the contact area on each asperity at a given scale. Then, any of the asperity contact models described earlier in this work can be used to find the contact area of each asperity as a function of the force. In this way one could include the effects of elasticity, plasticity, adhesion, sliding, and layered contact. However, since (3.90) and (3.91) must be solved iteratively and can be complicated to code, a closed form version of the multiscale is also provided and described in the following paragraphs.

3.2.1 Elastic Contact

Provided here is a simplified solution of the full multiscale model, which predicts nearly the same trends as the full multiscale model. It first assumes that the surface is constructed from a series of sinusoidal waves, with the small scales of roughness being stacked onto the tips of larger scale asperities. Now, imagine that the average pressure required to flatten the surface within the real area of contact must overcome all the scales of roughness within the real area of contact. This average pressure can easily be calculated from the average pressure needed to flatten a sinusoidal surface as described earlier by (3.25). Since the real area of contact is calculated by the contact force divided by this pressure, we have

$$A_r = \frac{F}{p^*} \tag{3.95}$$

Then, the real contact pressure, P_r, is equal to p^*. p^* is the pressure required to flatten the sine wave on the surface with the maximum asperity aspect ratio (Δ/λ) or B_{max}. Recall that Δ and λ are the amplitude and wavelength of the sinusoidal surfaces, respectively. B_{max} is found from the Fourier transform of a surface and comparing all the amplitude to wavelength ratios over all known scales of the surface. The real area of contact can be obtained then by substituting (3.8) into (3.18) or

$$(A_r)_{elastic} = \frac{F}{\sqrt{2}\pi E' B_{max}} \tag{3.96}$$

which is a very simple and yet effective way to predict the real area of contact. However, this equation does not include the effect of plasticity which is likely to occur in the contact of rough surfaces.

3.2.2 Elastic–Plastic Contact

Consider that for sinusoidal surfaces the critical ratio between the amplitude and wavelength is analytically derived as [79]

$$B_c = \frac{\Delta_c}{\lambda} = \frac{\sqrt{2}S_y}{3\pi E'} e^{\frac{2}{3}\nu} \tag{3.97}$$

where the smaller yield strength S_y from the surfaces in contact is used. Then, for multiscale rough surface contact, if $B_{max} < B_c$, the contact is elastic contact even for very high loads, and (3.96) should be used. Alternatively, if $B_{max} > B_c$, then a version of the model which considers elastic–plastic deformation should be used. Since this ratio defines the existence of plastic deformation in a rough surface

contact within the multiscale contact framework, an analytically derived multiscale plasticity index is

$$\psi_c = \frac{B_{\max}}{B_c} = \frac{3\pi E'}{\sqrt{2}e^{2/3\nu} \cdot S_y} \left(\frac{\Delta}{\lambda}\right)_{\max} \tag{3.98}$$

Note that when this plasticity index is below unity, no plastic deformation should occur, even when loaded to complete contact (i.e., no gaps between the surfaces).

However, in many cases the plasticity index will be well above unity, and so plasticity must be considered. For multiscale elastic–plastic contact, (3.95) is adjusted to

$$A_r = \frac{F}{p^*_{ep}} \tag{3.99}$$

Therefore, to calculate the real area for elastic–plastic multiscale contact, the relatively simple equation next can be used:

$$(A_r)_{elastic-pastic} = \frac{F}{\sqrt{2}\pi E' B_{max}} \left(\frac{\frac{12\pi E'}{\sqrt{2}S_y e^{\frac{2}{3\nu}}} B_{max} + 7}{11} \right) \tag{3.100}$$

Just as (3.96) can easily be used for elastic contact, (3.100) can easily be implemented to make a prediction of the real area of contact for rough surfaces in contact and deforming in the elastic–plastic regime. These closed form versions of the multiscale contact model are plotted in Fig. 3.19 as a function of B_{max} and the real contact pressure normalized by the yield strength. The initiation of plastic deformation as predicted by (3.97) is shown by a red line at $P_r/S_y = 0.83$ for a Poisson's ratio of $\nu = 0.33$. This threshold is found by simply substituting the critical amplitude, B_c, into p^*. Once this threshold is crossed, the pressure continues to increase with B_{max}, but at a more gradual slope. Nonetheless, the P_r/S_y continues to rise well past the ratio of 3, which for many years was considered the maximum obtainable pressure in the contact of rough surfaces. It is clear that the pressure can rise far past that, even in the typical range of engineering surfaces (also shown in Fig. 3.19).

Actually, this increase in the real contact pressure well past the traditional limit of $3 \cdot S_y$ is also observed in a few papers which observe what is coined as "asperity persistence." The asperity persistence is the measured ability of asperities to resist flattening even at very high pressures. As shown in the works by Childs [80], Uppal and Probert [81], Demkin and Izmailov [82], and Pullen and Williamson [83], the real contact pressure was sometimes measured to be as high as $6–10 \cdot S_y$ for aluminum surfaces of 2.25 μm to 6 μm in average roughness. Since the original surface data from these works was not readily available, this analysis is based solely on the limited data in Table 3.2. From the typical proportions shown in Table 3.2, the

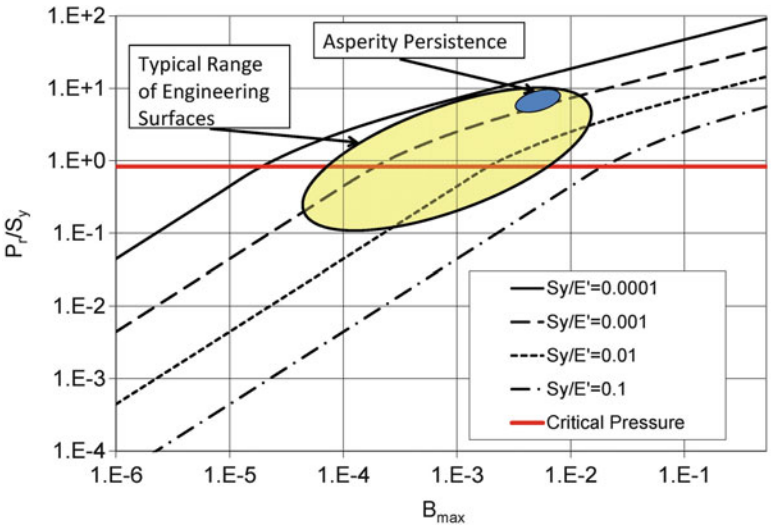

Fig. 3.19 The real contact pressure as predicted by the multiscale rough surface contact model

Table 3.2 Example roughness values and B_{max} values for four surfaces

Surface	R_q (μm)	B_{ave}	B_{max}
1	0.24	0.000257	0.000818
2	0.34	0.000181	0.00215
3	1.05	0.000525	0.00574
4	5.82	0.00182	0.00951

B_{max} values of these surfaces might be approximated as 0.006 (2.25 μm) and 0.01 (6 μm). Assuming aluminum to have approximate material properties of S_y/E'=0.001, it appears that the current model predicts the value of P_r/S_y for these two surfaces to be at 6–10 · S_y, as shown in Fig. 3.19.

It is more difficult to predict the surface separation between rough surfaces using the multiscale model approach. However, Wilson et al. [78] did show that reasonable predictions could be made by simply summing the deformed height of each scale in contact or

$$d = \sum_{i=1}^{i_{\max}} \left(\overline{\delta}\right)_i \tag{3.101}$$

where $\overline{\delta}$ is the deformed height of each asperity scale. Wilson et al. [78] and Johnson et al. [84] provide models to predict the surface separation for the contact of elastically deforming sinusoids. If one wishes to consider the contact of two identical surfaces, then the contact between them would be an axis of symmetry, and therefore, the surface separation will be the double of that predicted by (3.101). The multiscale model predicts that the surfaces will not come into significant contact

until they are in much closer proximity than the statistical models. Likewise, once the surfaces are in contact, the multiscale model predicts that the pressure will increase much more quickly as the surface separation decreases (i.e., the contact stiffness is much higher). This finding agrees with findings by Drinkwater et al. [85] who made measurements of the contact stiffness using acoustic methods.

3.3 Scale-Dependent Properties

When rough surfaces come into contact, the asperity contacts can be very small, even on the atomic scale. It is now well known that material properties can change significantly with scale so that the bulk properties of a material are different than the properties at the scale of contacting asperities. For instance, the yield strength of bulk materials is usually much smaller than the yield strength of nanoscale pillars [86] or nanowires [87]. One mechanism for this effect in metals is that as you reduce the scale, you may go below the scale of features such as grains and reach a state where the material is a stronger single lattice of atoms. Other material properties such as electrical and thermal conductivity can also change with scale. The scale-dependent properties can be included in the models of rough surface contact above as shown in these published works [88–90]. Recent works have also shown that even continuum-based models, if used in conjunction with an accurate material property model can on average accurately capture nanoscale contact mechanisms [91].

4 Conclusions

Contact mechanics is clearly an important and useful part of tribology and general science and engineering. It can help to predict the life and eventual failure on such components as bearings, gears, and wheels. It can also be used to model the contact between rough surfaces and then illuminate the mechanisms governing friction, wear, surface fatigue, and contact resistance. It can be a powerful tool but should still be used with caution, because predictions can often provide qualitatively accurate predictions but have significant quantitative error, especially when considering the contact of rough surfaces. Models exist not only to consider the normal contact of spheres and other geometries but also can include tangential loading, adhesion, and surface layers.

References

1. Archard JF (1957) Elastic deformation and the laws of friction. Proc R Soc Lond A 243:190–205
2. Tabor D (1951) The hardness of materials. Clarendon, Oxford

3. Greenwood JA, Williamson JBP (1966) Contact of nominally flat surfaces. Proc R Soc Lond A 295(1442):300–319
4. Johnson KL (1985) Contact mechanics. Cambridge University Press, New York
5. Johnson KL (1982) One hundred years of hertz contact. Proc Inst Mech Eng 196(1):363–378
6. Hamrock BJ (1994) Fundamentals of fluid film lubrication. Mcgraw-Hill, Inc., New York
7. Green I (2005) Poisson ratio effects and critical values in spherical and cylindrical Hertzian contacts. Int J Appl Mech Eng 10(3):451–462
8. Vijaywargiya R, Green I (2007) A finite element study of the deformation, forces, stress formation, and energy loss in sliding cylindrical contacts. Int J Non-Linear Mech 42:914–927
9. Chang WR, Etsion I, Bogy DB (1987) An elastic–plastic model for the contact of rough surfaces. ASME J Tribol 109(2):257–263
10. Zhao Y, Maletta DM, Chang L (2000) An asperity microcontact model incorporating the transition from elastic deformation to fully plastic flow. ASME J Tribol 122(1):86–93
11. Kogut L, Etsion I (2002) Elastic–plastic contact analysis of a sphere and a rigid flat. ASME J Appl Mech 69(5):657–662
12. Jackson RL, Green I (2005) A finite element study of elasto-plastic hemispherical contact. ASME J Tribol 127(2):343–354
13. Wadwalkar SS, Jackson RL, Kogut L (2010) A study of the elastic–plastic deformation of heavily deformed spherical contacts. IMechE Part J, J Eng Tribol 224(10):1091–1102
14. Jackson RL, Chusoipin I, Green I (2005) A finite element study of the residual stress and strain formation in spherical contacts. ASME J Tribol 127(3):484–493
15. Etsion I, Kligerman Y, Kadin Y (2005) Unloading of an elastic–plastic loaded spherical contact. Int J Solids Struct 42(13):3716–3729
16. Quicksall JJ, Jackson RL, Green I (2004) Elasto-plastic hemispherical contact models for various mechanical properties. IMechE J Eng Trib Part J 218(4):313–322
17. Jackson RL, Kogut L (2006) A comparison of flattening and indentation approaches for contact mechanics modeling of single asperity contacts. ASME J Tribol 128(1):209–212
18. Kogut L, Komvopoulos K (2004) Analysis of spherical indentation cycle of elastic-perfectly plastic solids. J Mater Res 19:3641–3653
19. Westergaard HM (1939) Bearing pressures and cracks. ASME J Appl Mech 6:49–53
20. Johnson KL, Greenwood JA, Higginson JG (1985) The contact of elastic regular wavy surfaces. Int J Mech Sci 27(6):383–396
21. Jackson RL, Streator JL (2006) A multiscale model for contact between rough surfaces. Wear 261(11–12):1337–1347
22. Shah S, Krithivasan V, Jackson RL (2011) An electro-mechanical contact analysis of a three-dimensional sinusoidal surface against a rigid flat. Wear 270:914–921
23. Krithivasan V, Jackson RL (2007) An analysis of three-dimensional elasto-plastic sinusoidal contact. Trib Lett 27(1):31–43
24. Jackson RL, Krithivasan V, Wilson WE (2008) The pressure to cause complete contact between elastic plastic sinusoidal surfaces. IMechE J Eng Trib Part J 222(7):857–864
25. Chaise T, Nélias D, Sadeghi F (2011) On the effect of isotropic hardening on the coefficient of restitution for single or repeated impacts using a semi-analytical method. Tribol Trans 54 (5):714–722
26. Israelachvili JN (1991) Intermolecular and surface forces, 2nd edn. Academic, San Diego, CA
27. Johnson KL, Kendall K, Roberts AD (1971) Surface energy and the contact of elastic solids. Proc Roy Soc Lond Ser A (Math Phys Sci) 324(1558):301–313
28. Bradley R (1932) The cohesive force between solid surfaces and the surface energy of solids. Phil Mag Ser 7 13(86):853–862
29. Derjaguin BV, Muller VM, Toporov YP (1975) Effect of contact deformations on adhesion of particles. J Colloid Interface Sci 53(2):314–326
30. Muller VM, Derjaguin BV, Toporov YP (1983) On two methods of calculation of the force of sticking of an elastic sphere to a rigid plane. Colloids Surf 7(3):251–259
31. Tabor D (1977) Surface forces and surface interactions. J Colloid Interface Sci 58(1):2–13

32. Maugis D (1992) Adhesion of spheres: the JKR-DMT transition using a dugdale model. J Colloid Interface Sci 150(1):243
33. Carpick RW, Ogletree DF, Salmeron M (1999) A general equation for fitting contact area and friction vs load measurements. J Colloid Interface Sci 211:395–400
34. Fuller KNG, Tabor D (1975) The effect of surface roughness on the adhesion of elastic solids. Proc R Soc Lond A Math Phys Sci 345:327–342
35. Liu SB et al (2005) An extension of the Hertz theory for three-dimensional coated bodies. Tribol Lett 18(3):303–314
36. Gittus J (1975) Creep Viscoelasticity and creep fracture in solids, Applied Science Publishers, London
37. Goedecke A, Jackson RL, Mock R (2010) Asperity creep under constant force boundary conditions. Wear 268(11):1285–1294
38. Brot C, Etsion I, Kligerman Y (2008) A contact model for a creeping sphere and a rigid flat. Wear 265(5):598–605
39. Tomlins P (1996) Comparison of different functions for modelling the creep and physical ageing effects in plastics. Polymer 37(17):3907–3913
40. Garofalo F (1965) Fundamentals of creep and creep-rupture in metals. Macmillan, New York
41. Goedecke A, Mock R (2009) Creep relaxation of an elastic-perfectly plastic hemisphere in fully plastic contact. ASME J Tribol 131:021407
42. Brot CC, Etsion I, Kligerman Y (2008) A contact model for a creeping sphere and a rigid flat. Wear 265(5–6):598–605
43. Persson B (2000) Theory of time-dependent plastic deformation in disordered solids. Phys Rev B 61(9):5949
44. Cattaneo C (1938) Sul contato di due corpo elastici. Atti Accad Naz Lincei Cl Sci Fis Mat Nat Rend 27:342–348, 434–436, 474–478
45. Etsion I (2010) Revisiting the Cattaneo–Mindlin concept of interfacial slip in tangentially loaded compliant bodies. ASME J Tribol 132(2):020801, 9 pages
46. Mindlin RD, Deresiewicz H (1953) Elastic spheres in contact under varying oblique forces. ASME Trans J Appl Mech 20:327–344
47. Chang WR, Etsion I, Bogy DB (1988) Static friction coefficient model for metallic rough surfaces. ASME J Tribol 110(1):57–63
48. Brizmer V, Kligerman Y, Etsion I (2007) Elastic–plastic spherical contact under combined normal and tangential loading in full stick. Tribol Lett 25(1):61–70
49. Jackson RL et al (2007) An analysis of elasto-plastic sliding spherical asperity interaction. Wear 262(1–2):210–219
50. Boucly V, Nelias D, Green I (2007) Modeling of the rolling and sliding contact between two asperities. J Tribol-Trans ASME 129(2):235–245
51. Mulvihill DM et al (2011) An elastic–plastic asperity interaction model for sliding friction. Tribol Int 44(12):1679–1694
52. Bush AW, Gibson RD, Thomas TR (1975) The elastic contact of rough surfaces. Wear 35:87–111
53. Dwyer-Joyce RS, Reddyhoff T, Zhu J (2011) Ultrasonic measurement for film thickness and solid contact in elastohydrodynamic lubrication. ASME J Tribol 133(3):031501
54. McBride JW, Cross KC (2008) An experimental investigation of the contact area between a glass plane and both metallic and carbon-nano-tube electrical contacts in proceedings of the 54th IEEE Holm conference on electrical contacts. Orlando, FL
55. Kotake S et al (2008) Evaluation of electrical contact area between metal and semiconductor using photo-induced current. Tribol Int 41(1):44–48
56. Jackson RL, Ghaednia H, Yasser AE, Bhavnani S, Knight R (2012) A closed-form multiscale thermal contact resistance model, components, packaging and manufacturing technology. IEEE Trans 2(7):1158–1171
57. Sainsot P, Jacq C, Nelias D (2002) A numerical model for elastoplastic rough contact. Comput Model Eng Sci 3(4):497–506

58. Wang F et al. (2009) A multi-Scale model for the simulation and analysis of elasto-plastic contact of real machined surfaces. ASME J Tribol 131:021409-1-6
59. Stanley HM, Kato T (1997) FFT-based method for rough surface contact. J Tribol Trans ASME 119(3):481–485
60. Whitehouse DJ, Archard JF (1970) The properties of random surfaces of significance in their contact. Proc R Soc Lond A 316:97–121
61. Jackson RL, Green I (2003) A statistical model of elasto-plastic asperity contact between rough surfaces in proceedings of the ASME/STLE international tribology conference. Preprint 2003-TRIB102
62. Polycarpou A, Etsion I (1999) Analytical approximations in modeling contacting rough surfaces. ASME J Tribol 121(2):234–239
63. Yu N, Polycarpou AA (2004) Combining and contacting of two rough surfaces with asymmetric distribution of asperity heights. J Tribol Trans ASME 126(2):225
64. Kogut L, Etsion I (2003) A finite element based elastic–plastic model for the contact of rough surfaces. Tribol Trans 46(3):383–390
65. Greenwood JA, Tripp JH (1971) The contact of two nominally flat rough surfaces. Proc Instn Mech Engrs Part J 185:625–633
66. Ciavarella M, Delfine G, Demelio G (2006) A "re-vitalized" greenwood and williamson model of elastic contact between fractal surfaces. J Mech Phys Solids 54(12):2569–2591
67. Greenwood JA (2006) A simplified elliptical model of rough surface contact. Wear 261 (2):191–200
68. McCool JI (1986) Comparison of models for the contact of rough surfaces. Wear 107(1):37–60
69. Mikic B (1971) Analytical studies of contact of nominally flat surfaces; effect of previous loading. J Lubr Technol Trans ASME 93(4):451–456
70. Sepehri A, Farhang K (2009) Closed-form equations for three dimensional elastic–plastic contact of nominally flat rough surfaces. J Tribol Trans ASME 131(4)041402–1–8
71. Jackson RL, Green I (2011) On the modeling of elastic contact between rough surfaces. Tribol Trans 54(2):300–314
72. McCool JI (1987) Relating profile instrument measurements to the functional performance of rough surfaces. ASME J Tribol 109(2):264–270
73. Front I (1990) The effects of closing force and surface. Roughness on leakage in radial face seals, MS Thesis. Technion, Israel Institute of Technology
74. Ciavarella M, Demelio G (2001) Elastic multiscale contact of rough surfaces: Archard's model revisited and comparisons with modern fractal models. J Appl Mech 68(3):496–498
75. Ciavarella M et al (2000) Linear elastic contact of the Weierstrass profile. Proc R Soc Lond A 456:387–405
76. Ciavarella M, Murolo G, Demelio G (2006) On the elastic contact of rough surfaces: numerical experiments and comparisons with recent theories. Wear 261(10):1102–1113
77. Almeida L et al (2007) Laterally actuated multicontact MEMS relay fabricated using MetalMUMPS process: experimental characterization and multiscale contact modeling. J Micro/Nanolith MEMS MOEMS 6(2):023009
78. Wilson WE, Angadi SV, Jackson RL (2010) Surface separation and contact resistance considering sinusoidal elastic–plastic multi-scale rough surface contact. Wear 268(1–2):190–201
79. Jackson RL (2010) An analytical solution to an Archard-type fractal rough surface contact model. Tribol Trans 53(4):543–553
80. Childs THC (1977) The persistence of roughness between surfaces in static contact. Proc R Soc Lond A 353(1672):35–53
81. Uppal AH, Probert SD (1973) Plastic contact between a rough and a flat surface. Wear 23 (2):173–184
82. Demkin NB, Izmailov VV (1975) Plastic contact under high normal pressure. Wear 31 (2):391–402
83. Pullen J, Williamson JBP (1972) On the plastic contact of rough surfaces. Proc R Soc Lond A 327(1569):159–173

84. Johnson KL, Greenwood JA, Higginson JG (1985) The contact of elastic regular wavy surfaces. Int J Mech Sci 27(6):383–396
85. Drinkwater BW, Dwyer-Joyce RS, Cawley P (1996) A study of the interaction between ultrasound and a partially contacting solid—solid interface. in mathematical, physical and engineering sciences. The Royal Society
86. Greer JR, Nix WD (2005) Size dependence of mechanical properties of gold at the sub-micron scale. Appl Phys A: Mater Sci Process 80(8):1625–1629
87. Hyde B, Espinosa HD, Farkas D (2005) An atomistic investigation of elastic and plastic properties of Au nanowires. J Minerals Metals Mater 57(9):62–66
88. Almeida L et al (2006) Study of the electrical contact resistance of multi-contact MEMS relays fabricated using the MetalMUMPs process. J Micromech Microeng 16(7):1189–1194
89. Jackson RL (2006) The effect of scale dependant hardness on elasto-plastic asperity contact between rough surfaces. STLE Tribol Trans 49(2):135–150
90. Jackson RL, Bhavnani SH, Ferguson TP (2006) A multi-scale model of thermal contact resistance between rough surfaces (IMECE2006-15277). In ASME international mechanical engineering congress and exposition. Chicago, IL
91. Wang H et al (2010) Nanoindentation modeling of a nanodot-patterned surface on a deformable substrate. Int J Solids Struct 47(22–23):3203–3213

Exercises

1. If a spherical shaped surface and a sinusoidal or wavy shaped surface with identical material properties are both brought into contact with a flat surface, and the contact force is continually increased, which shape will ultimately have the highest contact pressure.

   For a sphere with the following properties, determine if the sphere will yield. Also determine the critical interference which will initiate yielding.
2. A person throws a bowling ball in the air and it lands with a force of 1 kN on the wooden lane. Assume that the bowling ball (diameter = 21.6 cm) properties are $E = 300$ GPa, $v = 0.4$ and the wood lane $E = 1$ GPa, and $v = 0.25$. Find the maximum real area of contact and estimate the combined maximum deflection (interference) of the ball and wood during contact.
3. Determine the maximum von Mises stress for a loaded sphere at z = 0.48a. Solve these equations and then estimate if the sphere will yield if it has the following properties:

$$R = 100\,\mu m, E = 100\,GPa, v = 0.33, S_y = 0.5\,GPa, \text{and the load is 1 N.}$$

4. Solve the Greenwood and Williamson model using the assumption in class that

$$\varphi(z) = \frac{2}{\sigma_s}\exp\left(-\frac{2}{\sigma_s}z\right)$$

If the surface parameters are given as ($\eta = 10^{11}/\text{m}^2$, $R = 20\mu m$, $\sigma = 0.2\mu m$, $E = 200\,GPa$, $v = 0.33$, $S_y = 0.5\,GPa$), plot the curves *of* A_r/A_n versus $d, W/E/A_n$

Table 3.3 The MTH model parameters for different polymers

Material	C_2	C_3	E [Mpa]
PTFE	2	0.211	420
Delrin	1.101	0.278	3,100
Bakelite	1.695	0.232	2,500
Nylon-6	1.266	0.338	3,600
Polypropylene	1.607	0.173	1,520

versus d, and A_r/A_n versus $F/E/A_n$. Compare these results to results obtained from the model by Green (2002) for the same surface parameters.

5. Assuming the material properties of a typical steel ($E = 200$ GPa, $v = 0.33$, $S_y = 0.5$ GPa, ρ=7,850 kg/m^3), find the smallest size sphere that will not deform *plastically* under its own weight when set on a rigid flat surface.
6. Calculate the radius of contact under no applied load (a_0), based on the JKR model.
7. Calculate the radius of contact right before separation (a_s) and write a_s as a function of a_0 (see problem 6).
8. Considering the creep process of the polymer Delrin in contact with a rigid flat surface, calculate the creep displacement and contact area of the single asperity of this polymer after 350 min under a constant force.

   We know that after 600 min the creep displacement of the single asperity is 8 μm. You can use the parameters in Table 3.3 for required information.
9. In a compression testing, a soft metal sample would be flattening against rigid flat surface (sapphire). The mechanical properties of the sample are as below: $E_1 = 12.74$ GPa, $E_2 = 345$ GPa, $v_1 = 0.4498$, $v_2 = 0.29$, $S_y = 1.4$ Mpa, E_1, E_2, v_1, v_2 are the elastic moduli and Poisson's ratios of the sample and sapphire, respectively. S_y is the yield strength of the sample. The max value of ratio amplitude/wavelength is $B_{max} = 0.0011$. Please calculate the real area when load F = 300N is applied.

Solutions

1. The pressure in a sinusoidal contact should increase past that of a spherical contact under heavy loads. Since the boundary conditions at the base of these geometries are different, the sphere will become a pillar and the sinusoidal surface will become two flat surfaces in contact.
2. The effective radius and elastic modulus for the contact is calculated as

$$E' = \left(\frac{1-\nu_1^2}{E_1}{}^{1} + \frac{1-\nu_2^2}{E_2}\right)^{-1} = 1.06GPa$$

$$\frac{1}{R} = \frac{1}{R_1} + \frac{1}{R_2} = 0.108m$$

From $F = \frac{4}{3}E'\sqrt{R}(\omega)^{3/2}$, the interference is 0.000167 m.
From $A = \pi R\omega = \pi a^2$, the contact radius is 0.00424 m.

3. Use the following equations provided earlier in the book to predict the critical contact force and interference:

$$C = 1.295\exp(0.736v)$$

$$\mathrm{C} = 1.651$$

$$P_c = \frac{4}{3}\left(\frac{R}{E'}\right)^2\left(\frac{C}{2}\pi \cdot S_y\right)^3$$

$$= \frac{4}{3}\left(\frac{100 \cdot 10^{-6}m}{112 \cdot 10^9 N/m^2}\right)^2\left(\frac{1.651}{2}\pi \cdot 500 \cdot 10^6 N/m^2\right)^3 = 0.0023N$$

Clearly, the applied for 1 N is much larger than the critical force, and therefore, the sphere will yield. In addition,

$$\omega_c = \left(\frac{\pi \cdot C \cdot S_y}{2E'}\right)^2 R = 0.013\mu m$$

4. Find the paper by Polycarpou and Etsion for the full derivation. This in itself is good practice.
5. Using the critical force equation given in the text and finding the force by multiplying the volume of the sphere x density x gravitational constant to obtain

$$P_c = \frac{4}{3}\left(\frac{R}{E'}\right)^2\left(\frac{C}{2}\pi \cdot S_y\right)^3 = \frac{4\pi}{3}R^3\rho g$$

Solving for R,

$$R = \frac{1}{\rho g}\left(\frac{\pi}{E'}\right)^2\left(\frac{C}{2}S_y\right)^3 = 0.186m$$

6. From the JKR model,

$$a^3 = \frac{R}{E}\left[F + 3\pi RW_{12} + \sqrt{6\pi RW_{12}F + (3\pi RW_{12})^2}\right]$$

Setting F = 0 results in

$$a^3 = \frac{R}{E}\left[F + 3\pi RW_{12} + \sqrt{6\pi RW_{12}F + (3\pi RW_{12})^2}\right]$$

$$a = \sqrt[3]{\frac{R}{E}(6\pi R W_{12})}$$

7. Recall that the pull off force is

$$F_s = -3\pi R W_{12}/2$$

Substituting this into the JKR model,

$$a = \sqrt[3]{\frac{R}{E}\left(\frac{3}{2}\pi R W_{12}\right)}$$

8. According to the information given in the problem,

$$R = 1mm$$
$$\omega_{cr}(600) = 8\mu m$$

From Table 3.3, for polymer Derlin,

$$C_2 = 1.101, C_3 = 0.278$$
$$\omega_{cr}(t) = 8 \times \left(\frac{350}{600}\right)^{(0.71\times 0.278+0.03)} = 7.077\mu m$$
$$A_{cr}(350) = 1.101 \times \pi \times 1000 \times 8 \times \left(\frac{350}{500}\right)^{0.71\times 0.278+0.03} = 0.02448mm^2$$

9. First, we can calculate effective elastic modulus:

$$E' = \left(\frac{1-\nu_1^2}{E_1} + \frac{1-\nu_2^2}{E_2}\right)^{-1} = \left(\frac{1-0.4498^2}{12.74\times 10^9} + \frac{1-0.29^2}{345\times 10^9}\right)^{-1} = 1.5322\times 10^{10}\text{Pa}$$

Then, critical ratio

$$B_c = \frac{\sqrt{2}}{3\pi}\frac{S_y}{E'}e^{\frac{2}{3}y} = \frac{\sqrt{2}}{3\times\pi}\frac{1.4\times 10^6}{1.5322\times 10^{10}} \times e^{\frac{2}{3}\times(0.4489)} = 1.8505\times 10^{-5}$$

Compare to the value of B_{max}
$B_{max} > B_c$, it means elastic–plastic contact.
When $F = 300N$, the real contact area can be calculated by

$$(A_r)_{elastic-pastic} = \frac{F}{\sqrt{2}\pi E' B_{max}} \left(\frac{\frac{12\pi E'}{\frac{2}{3} v_2} B_{max} + 7}{\frac{\sqrt{2} S_y e}{11}} \right)^{\frac{3}{5}}$$

$$= \frac{300}{\sqrt{2} \times \pi \times 1.5322 \times 10^{10} \times 0.0011} \left(\frac{\frac{12 \times \pi \times 1.5322 \times 10^{10}}{\frac{2}{3} \times 0.4498} \times 0.0011 + 7}{\frac{\sqrt{2} \times 1.4 \times 10^{6} \times e}{11}} \right)^{\frac{3}{5}}$$

$$= 2.5773 \times 10^{-5} m^2$$